CHAPTER IV

RESULTS AND DISCUSSION

4.1 Photocatalyst Characterizations

4.1.1 TG-DTA Results

The TG-DTA curves were used to study the thermal decomposition behavior of the $0.97TiO_2$-$0.03SiO_2$, $0.93TiO_2$-$0.07ZrO_2$, and $SrTi_{0.93}Zr_{0.07}O_3$ dried gel photocatalysts. Figure 4.1 exemplifies the TG-DTA curves of the dried pure TiO_2, $0.97TiO_2$-$0.03SiO_2$, and $0.93TiO_2$-$0.07ZrO_2$ gels. The DTA curves show three main exothermic regions. The first exothermic region at the temperature lower than 150 °C corresponds to the release of physisorbed water molecules. The second exothermic region between 150 °C and 320 °C is due to the burnout of the LAHC surfactant molecules. The third exothermic region between 320 °C and 500 °C plausibly results in not only from the crystallization process of the photocatalysts but also the removal of organic remnants and chemisorbed water molecules (Hague *et al.*, 1994). The TG curves show that the weight losses of $0.97TiO_2$-$0.03SiO_2$ and $0.93TiO_2$-$0.07ZrO_2$ mixed oxide gels are ended at a temperature of approximately 500 °C, which is sufficient for both the complete surfactant removal and the photocatalyst crystallization process. Therefore, the calcination temperature of 500 °C was used to study the physicochemical properties and consequent photocatalytic hydrogen production activity of the synthesized $0.97TiO_2$-$0.03SiO_2$ and $0.93TiO_2$-$0.07ZrO_2$ photocatalysts.

(a)

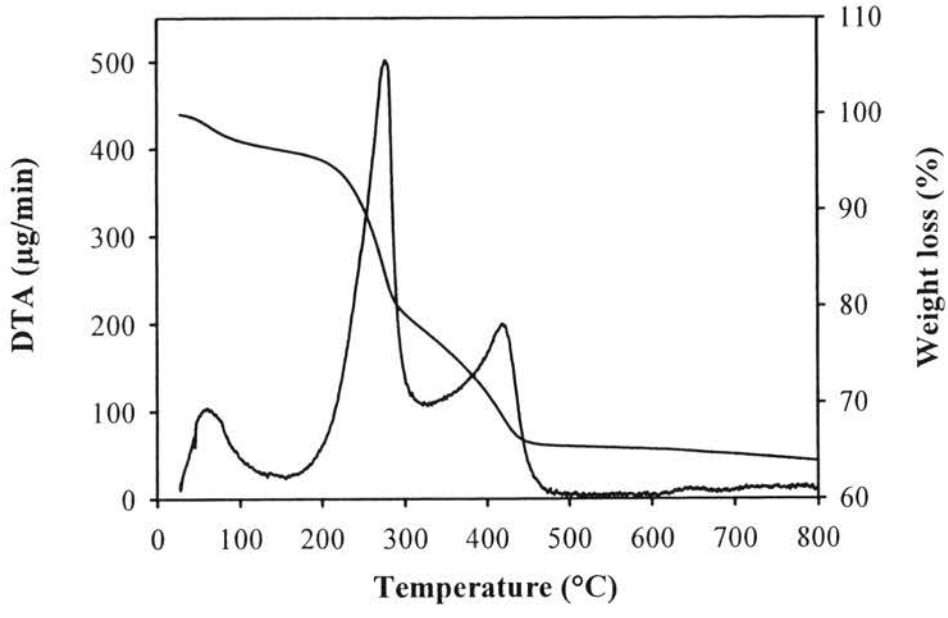
DTA (µg/min)
Weight loss (%)
Temperature (°C)
0
100
200
300
400
500
600
700
800
60
70
80
90
100
110

(b)

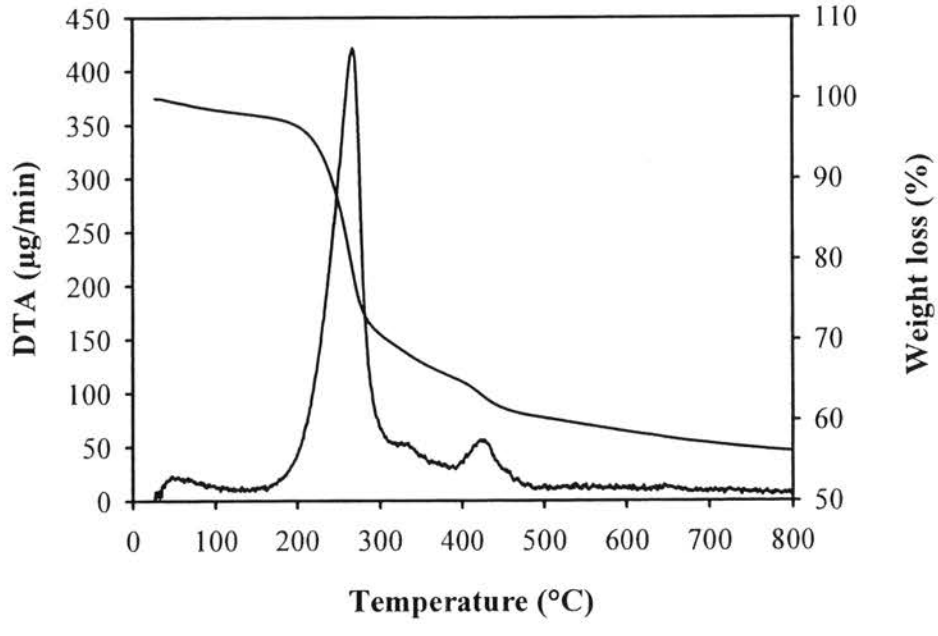
DTA (µg/min)
Weight loss (%)
Temperature (°C)
0
50
100
150
200
250
300
350
400
450
50
60
70
80
90
100
110

(c)

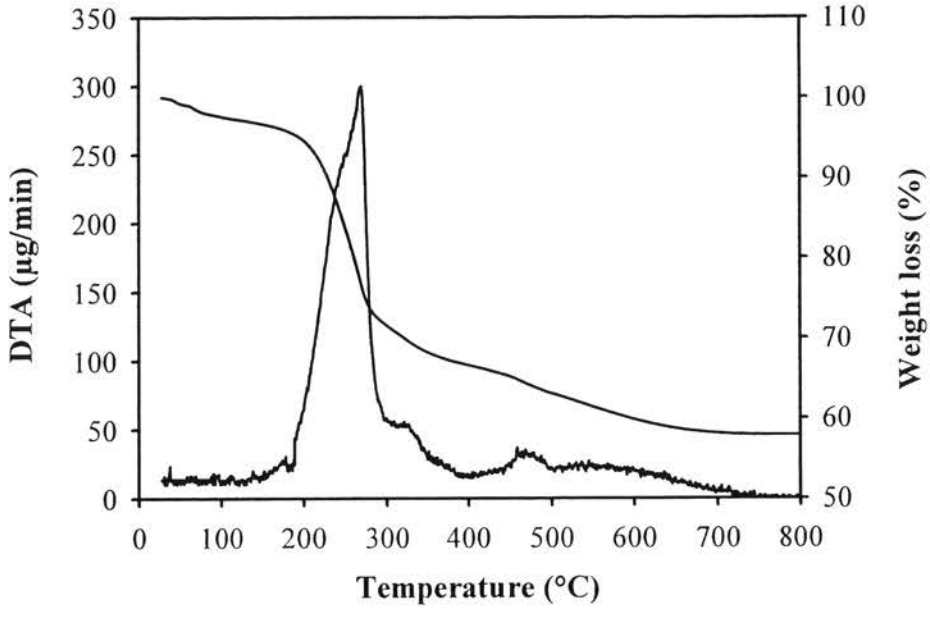

Figure 4.1 TG-DTA curves of the dried synthesized (a) pure TiO_2, (b) $0.97TiO_2$-$0.03SiO_2$, and (c) $0.93TiO_2$-$0.07ZrO_2$ photocatalysts.

Table 4.1 Thermal decomposition results of the dried synthesized pure TiO_2, $0.97TiO_2$-$0.03SiO_2$, and $0.93TiO_2$-$0.07ZrO_2$ mixed oxide photocatalysts from TG-DTA analysis

Photocatalyst	Position of exothermic peak (°C)			Corresponding weight loss (wt.%)			
	1st region	2nd region	3rd region	1st region	2nd region	3rd region	Total
TiO_2	30-150	150-320	320-500	1.77	19.37	14.61	35.75
$0.97TiO_2$-$0.03SiO_2$	30-150	150-320	320-500	1.99	25.06	11.79	38.84
$0.93TiO_2$-$0.07ZrO_2$	30-150	150-320	320-500	2.25	29.33	7.65	39.23

Figure 4.2 exemplifies the TG-DTA curves of the dried synthesized $SrTiO_3$ and $SrTi_{0.93}Zr_{0.07}O_3$ gels. The DTA curves also show three main exothermic regions (Khunrattanaphon *et al.*, 2011). The first exothermic region at the temperature lower than 190 °C corresponds to the removal of physisorbed water and EtOH molecules. The second exothermic region between 190 °C and 570 °C is due to the burnout of the LAHC surfactant molecules. The third exothermic region between 570 °C and 700°C is attributed to the removal of organic remnants and chemisorbed water molecules. The TG results reveal that the weight loss of the dried $SrTi_{0.93}Zr_{0.07}O_3$ gel is ended at a temperature approximately 700 °C, which is sufficient for both the complete surfactant removal and the photocatalyst crystallization process. Therefore, the calcination temperature of 700 °C was used to study the physicochemical properties and consequent photocatalytic hydrogen production activity of the synthesized $SrTi_{0.93}Zr_{0.07}O_3$ photocatalyst.

(a)

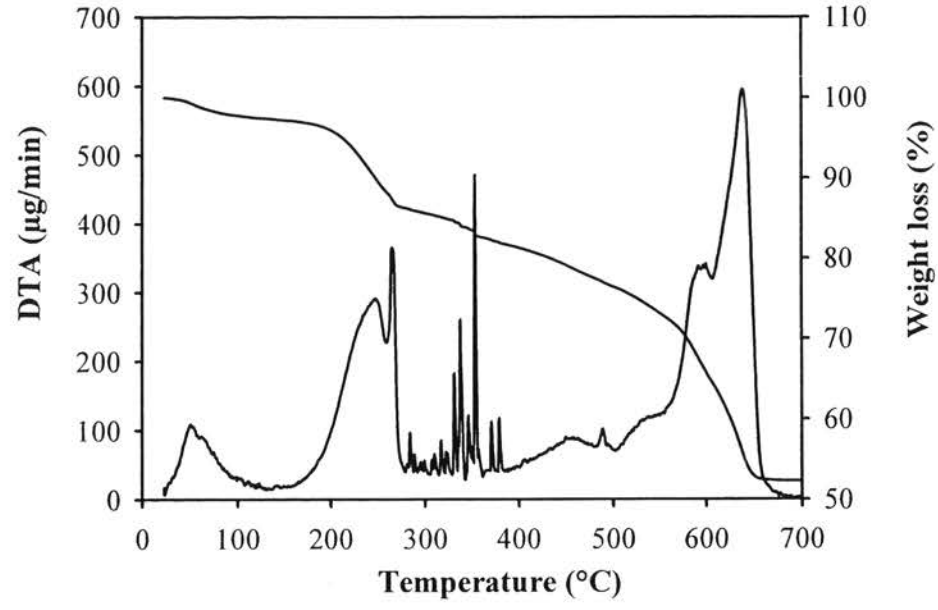

(b)

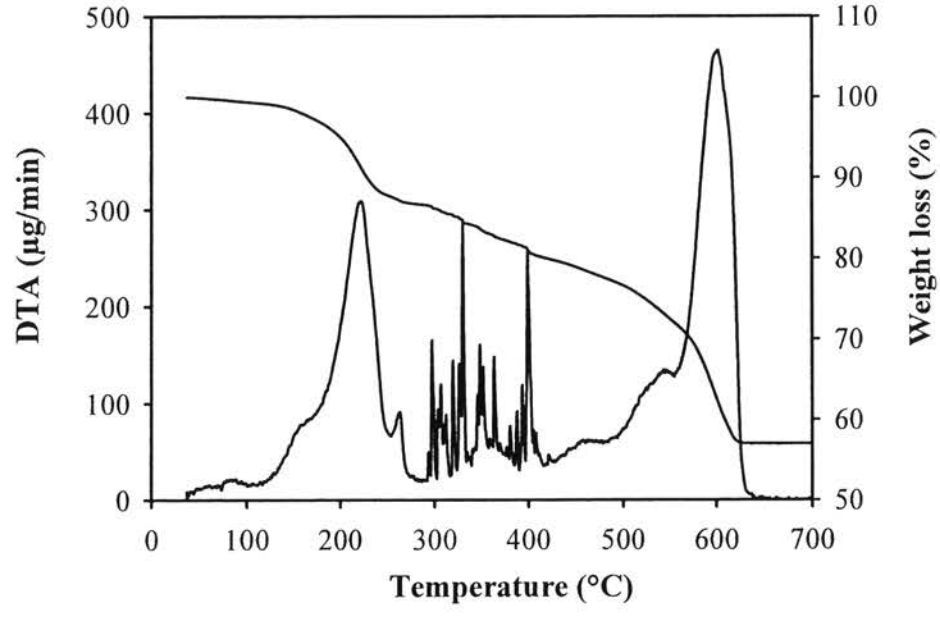

Figure 4.2 TG-DTA curves of the dried synthesized (a) $SrTiO_3$ and (b) $SrTi_{0.93}Zr_{0.07}O_3$ photocatalysts.

Table 4.2 Thermal decomposition results of the dried synthesized $SrTiO_3$ and $SrTi_{0.97}Zr_{0.03}O_3$ photocatalysts from TG-DTA analysis

Photocatalyst	Position of exothermic peak (°C)			Corresponding weight loss (wt.%)			
	1st region	2nd region	3rd region	1st region	2nd region	3rd region	Total
$SrTiO_3$	25-190	190-570	570-700	3.94	20.93	21.8	46.67
$SrTi_{0.97}Zr_{0.03}O_3$	25-190	190-570	570-700	3.42	21.42	17.40	42.24

4.1.2 N_2 Adsorption-Desorption Results

The N_2 adsorption-desorption analysis was used to verify the mesoporosity of the $0.97TiO_2$-$0.03SiO_2$, $0.93TiO_2$-$0.07ZrO_2$, and $SrTi_{0.93}Zr_{0.07}O_3$ photocatalysts with bimetallic Pt-Ag loadings. The adsorption-desorption isotherms exhibit the characteristic behavior of the structure of powder, which is composed of an assembly of particles with uniform pore opening. The isotherms of the pure TiO_2, $0.97TiO_2$-$0.03SiO_2$, $0.93TiO_2$-$0.07ZrO_2$, and bimetallic Pt-Ag-loaded photocatalysts calcined at 500 °C are shown in Figures 4.3-4.5. All of the samples exhibit typical IUPAC type IV pattern with H2-type hysteresis loop, which is the major characteristic of a mesoporous material (mesoporous size between 2 and 50 nm) according to the classification of IUPAC (Rouquerol *et al.*, 1999). A sharp increase in the adsorption curves at a high relative pressure (P/P_0) implies a capillary condensation of N_2 molecules inside the mesopores, implying the well-uniform mesopores and narrow pore size distributions since the P/P_0 position of the inflection point is directly related to the pore dimension. The insets of Figures 4.3-4.5 show the pore size distributions calculated from the desorption branch of the isotherms by the

DH method. The pure TiO_2, $0.97TiO_2$-$0.03SiO_2$, and $0.93TiO_2$-$0.07ZrO_2$ photocatalysts without and with bimetallic Pt-Ag loadings have quite narrow pore size distributions entirely locating in the mesoporous region (between 2 and 50 nm), implying a good quality of the samples. Table 4.3 shows the textural properties obtained from the N_2 adsorption-desorption analysis of the pure TiO_2, $0.97TiO_2$-$0.03SiO_2$, and $0.93TiO_2$-$0.07ZrO_2$ photocatalysts calcined at 500 °C. It is clearly observed that the incorporation of SiO_2 and ZrO_2 into TiO_2 resulted in an increase in specific surface area. For example, by incorporating 3 mol% SiO_2 and 7 mol% ZrO_2 into TiO_2 to obtain the $0.97TiO_2$-$0.03SiO_2$ and $0.93TiO_2$-$0.07ZrO_2$, the specific surface area increased from 63.7 to 161.6 $m^2 \cdot g^{-1}$ and 102.1 $m^2 \cdot g^{-1}$, respectively.

The $SrTiO_3$ and $SrTi_{0.93}Zr_{0.07}O_3$ photocatalysts without and with bimetallic Pt-Ag loadings also have quite narrow pore size distributions entirely locating in the mesoporous region (between 2 and 50 nm), identifying the good quality of the samples, as shown in Figures 4.6-4.7. The textural properties from the N_2 adsorption-desorption analysis of the $SrTiO_3$ and $SrTi_{0.93}Zr_{0.07}O_3$ photocatalysts calcined at 700 °C are shown in Table 4.3. It can be implied that the incorporation of ZrO_2 into $SrTiO_3$ resulted in an increase in specific surface area. The specific surface area increased from 4.5 to 8.4 $m^2 \cdot g^{-1}$. The presence of this second metal oxide with appropriate amounts could retard the crystallization process and affect the growth of bulk material, which was confirmed by the XRD analysis later, resulting in higher specific surface areas of the mixed oxide photocatalysts (Schattka *et al.*, 2002).

(a)

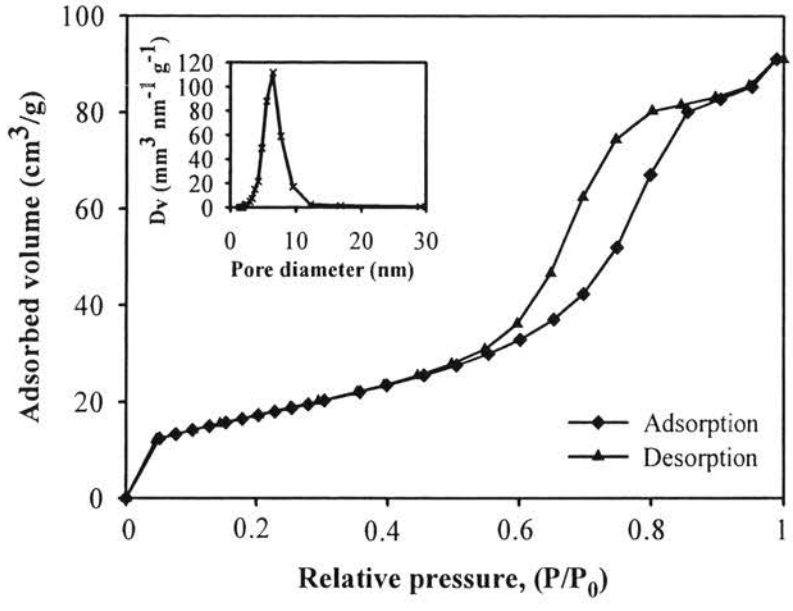
Adsorbed volume (cm3/g)
Relative pressure, (P/P0)
Adsorption
Desorption
Dv (mm3 nm-1 g-1)
Pore diameter (nm)

(b)

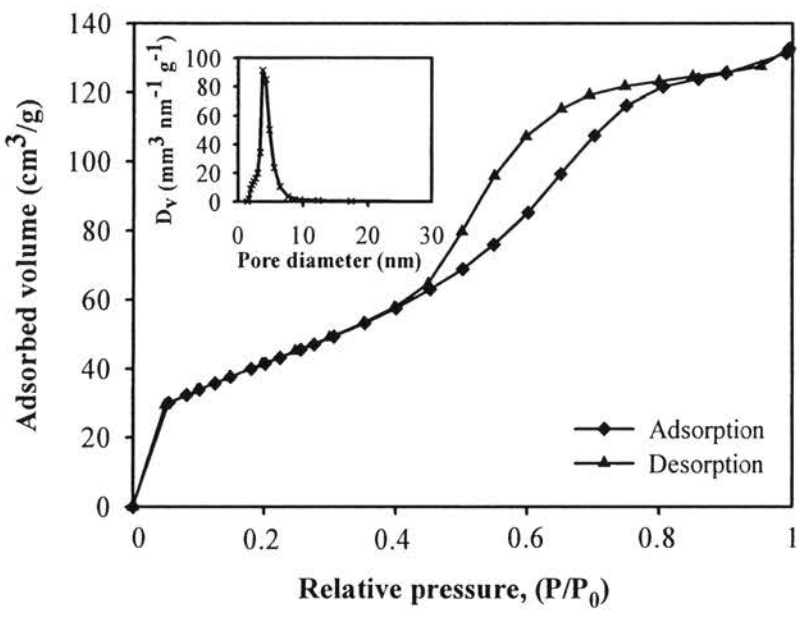
Adsorbed volume (cm3/g)
Relative pressure, (P/P0)
Adsorption
Desorption
Dv (mm3 nm-1 g-1)
Pore diameter (nm)

(c)

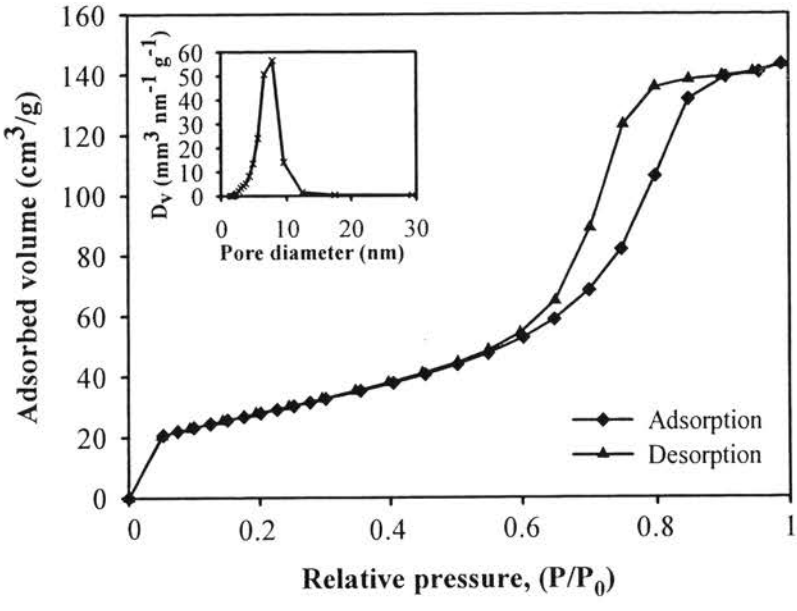

Figure 4.3 N_2 adsorption-desorption isotherms and pore size distributions (inset) of the synthesized mesoporous-assembled photocatalysts calcined at 500 °C: (a) pure TiO_2, (b) $0.97TiO_2$-$0.03SiO_2$ and (c) $0.93TiO_2$-$0.07ZrO_2$.

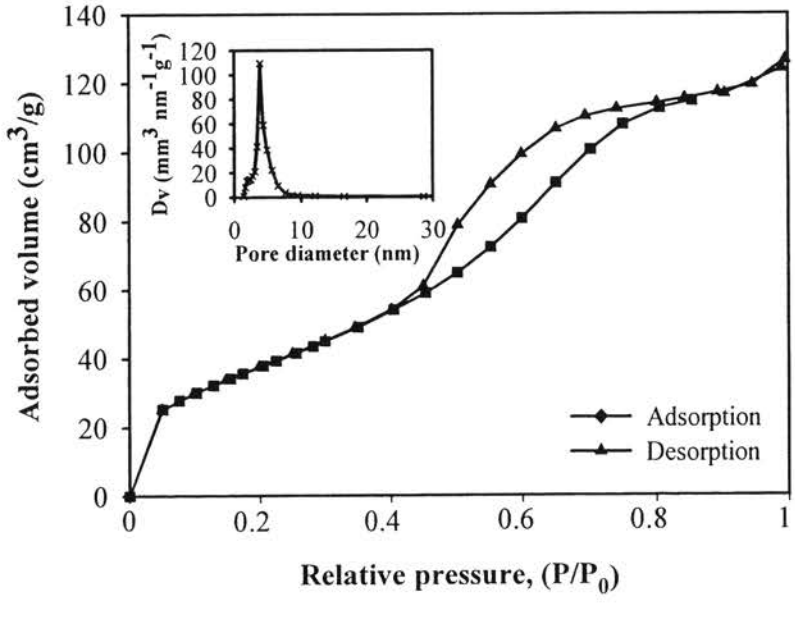

Figure 4.4 N_2 adsorption-desorption isotherms and pore size distribution (inset) of the synthesized 1.25 wt.% Pt-0.25 wt.% Ag-loaded mesoporous-assembled $0.97TiO_2$-$0.03SiO_2$ photocatalyst calcined at 500 °C.

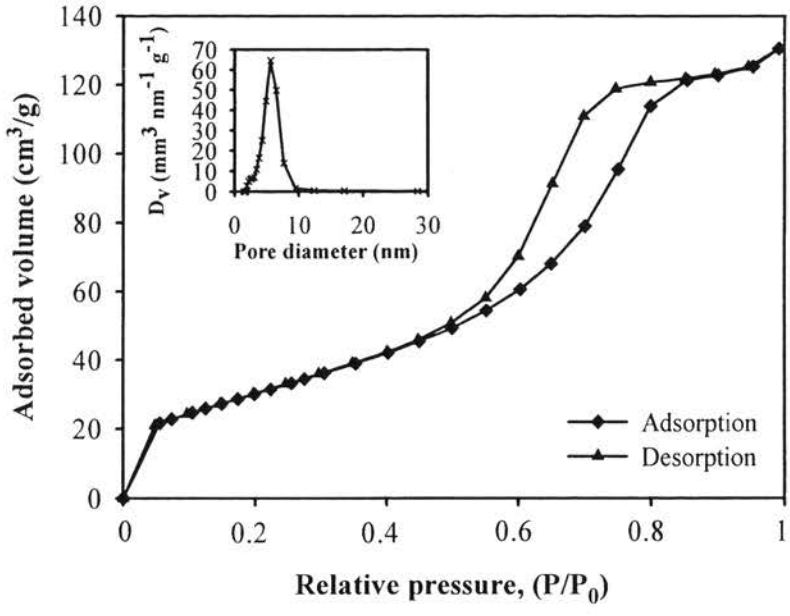

Figure 4.5 N_2 adsorption-desorption isotherms and pore size distribution (inset) of the synthesized 1.25 wt.% Pt-0.25 wt.% Ag-loaded mesoporous-assembled $0.93TiO_2$-$0.07ZrO_2$ photocatalyst calcined at 500 °C.

(a)

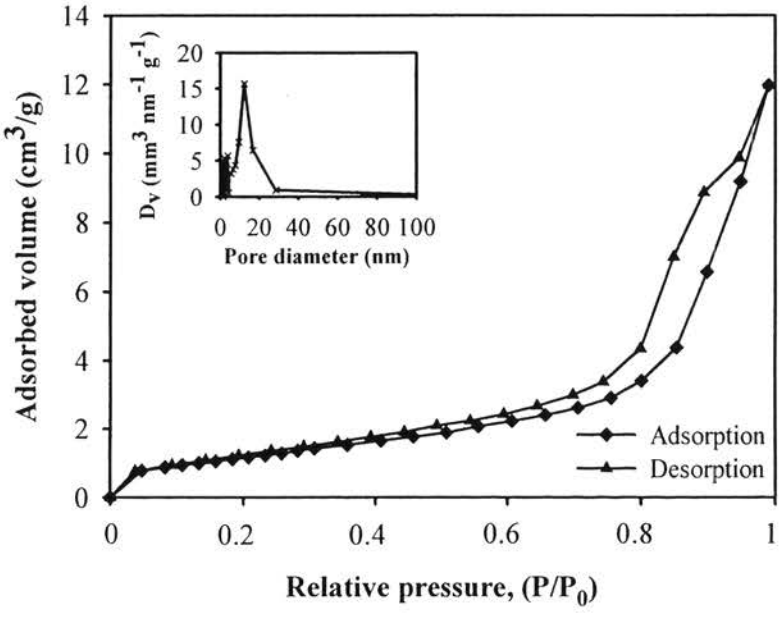

(b)

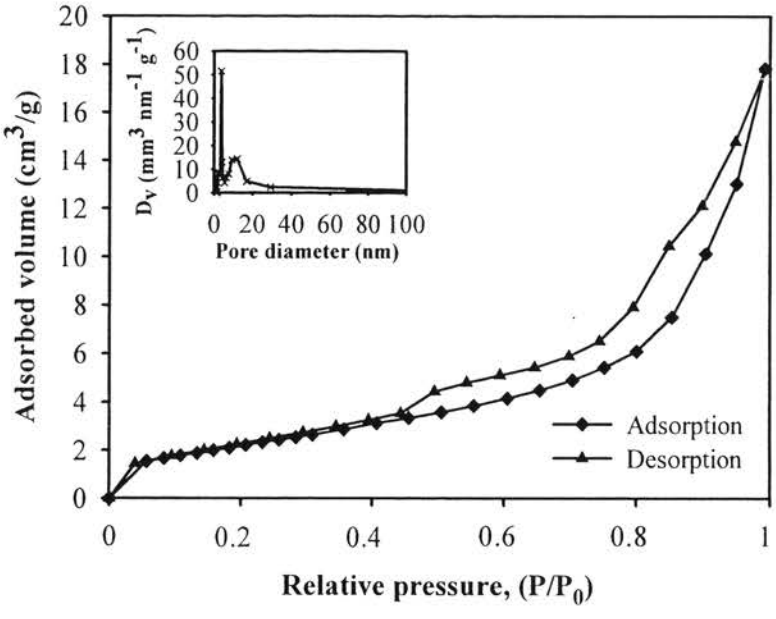

Figure 4.6 N_2 adsorption-desorption isotherms and pore size distributions (inset) of the synthesized mesoporous-assembled photocatalysts calcined at 700 °C: (a) $SrTiO_3$ and (b) $SrTi_{0.93}Zr_{0.07}O_3$.

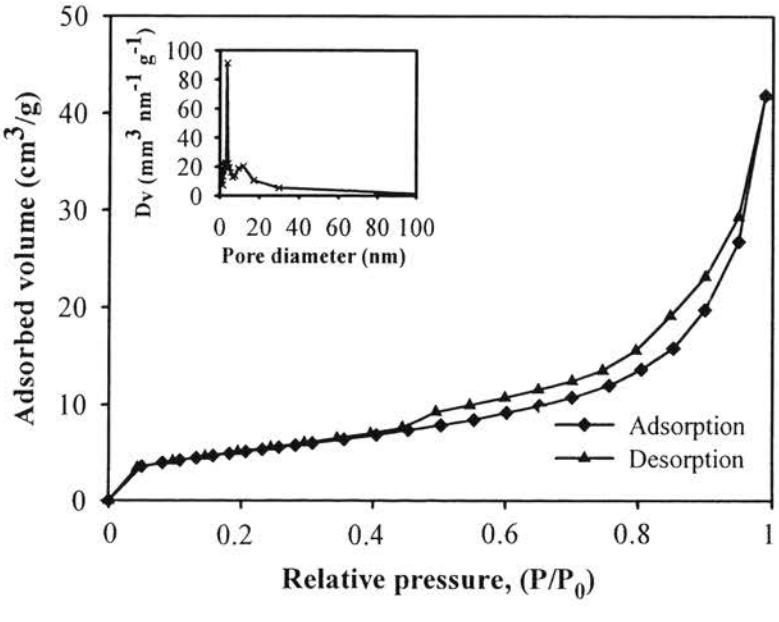

Figure 4.7 N_2 adsorption-desorption isotherms and pore size distribution (inset) of the synthesized 1.25 wt.% Pt-0.25 wt.% Ag-loaded mesoporous-assembled $SrTi_{0.93}Zr_{0.07}O_3$ photocatalyst calcined at 700 °C.

Table 4.3 N_2 adsorption-desorption results of the synthesized mesoporous-assembled pure TiO_2, $0.97TiO_2$-$0.03SiO_2$, $0.93TiO_2$-$0.07ZrO_2$, $SrTiO_3$, and $SrTi_{0.93}Zr_{0.07}O_3$ photocatalysts

Photocatalyst	Calcination temperature (°C)	Specific surface area ($m^2 \cdot g^{-1}$)	Mean mesopore diameter (nm)	Total pore volume ($cm^3 \cdot g^{-1}$)
Pure TiO_2	500	63.7	6.52	0.141
$0.97TiO_2$-$0.03SiO_2$	500	161.6	3.83	0.203
$0.93TiO_2$-$0.07ZrO_2$	500	102.1	7.83	0.227
$SrTiO_3$	700	4.5	10.30	0.019
$SrTi_{0.93}Zr_{0.07}O_3$	700	8.4	3.78	0.028

Table 4.4 shows the summary of textural properties of the synthesized bimetallic Pt-Ag-loaded mesoporous-assembled $0.97TiO_2$-$0.03SiO_2$, $0.93TiO_2$-$0.07ZrO_2$, and $SrTi_{0.93}Zr_{0.07}O_3$ photocatalysts. The results reveal that the specific surface areas of the 1.25 wt.% Pt-0.25 wt.% Ag-loaded $0.97TiO_2$-$0.03SiO_2$, 1.25 wt.% Pt-0.25 wt.% Ag-loaded $0.93TiO_2$-$0.07ZrO_2$, and the 1.25 wt.% Pt-0.25 wt.% Ag-loaded $SrTi_{0.93}Zr_{0.07}O_3$ were higher than such photocatalysts with other bimetallic Pt-Ag loadings. The specific surface areas of the bimetallic Pt-Ag-loaded mesoporous-assembled photocatalysts were slightly higher than that of the unloaded photocatalysts. This can be possibly caused by the high dispersion of the loaded bimetallic Pt-Ag on the photocatalysts.

Table 4.4 N_2 adsorption-desorption results of the synthesized bimetallic Pt-Ag-loaded mesoporous-assembled $0.97TiO_2$-$0.03SiO_2$, $0.93TiO_2$-$0.07ZrO_2$, and $SrTi_{0.93}Zr_{0.07}O_3$ photocatalysts

Photocatalyst	Pt loading (wt.%)	Ag loading (wt.%)	Specific surface area ($m^2 \cdot g^{-1}$)	Mean mesopore diameter (nm)	Total pore volume ($cm^3 \cdot g^{-1}$)
$0.97TiO_2$-$0.03SiO_2$	1.5	0	145.0	3.83	0.192
	1.25	0.25	158.1	3.83	0.216
	1	0.5	151.9	3.82	0.204
	0.75	0.75	150.2	3.81	0.202
	0.5	1	139.5	3.84	0.181
	0.25	1.25	152.5	3.82	0.201
	0	1.5	154.6	3.83	0.203
$0.93TiO_2$-$0.07ZrO_2$	1.5	0	113.3	5.64	0.211
	1.25	0.25	119.1	5.65	0.215
	1	0.5	114.6	5.63	0.219
	0.75	0.75	113.9	5.62	0.219
	0.5	1	113.8	6.58	0.215
	0.25	1.25	113.7	5.63	0.212
	0	1.5	117.1	5.64	0.215
$SrTi_{0.93}Zr_{0.07}O_3$	1.5	0	18.3	3.79	0.070
	1.25	0.25	18.9	3.79	0.065
	1	0.5	17.9	3.80	0.065
	0.75	0.75	18.4	3.82	0.066
	0.5	1	18.3	3.81	0.059
	0.25	1.25	15.5	3.84	0.063
	0	1.5	18.2	3.81	0.064

4.1.3 XRD Results

The XRD patterns of the $0.97TiO_2$-$0.03SiO_2$ and $0.93TiO_2$-$0.07ZrO_2$ calcined at 500 °C show crystalline structure of the pure anatase phase. The dominant peaks at 2θ of about 25.2°, 37.9°, 48.3°, 53.8°, and 55.0°, which represent the indices of (101), (103), (200), (105), and (211) planes, respectively (Smith, 1960), correspond to the crystalline anatase pure TiO_2, as shown in Figure 4.8. Figure 4.9 reveals the XRD pattern of the $SrTi_{0.93}Zr_{0.07}O_3$ photocatalyst calcined at 700 °C shows crystalline structure of the cubic phase. The dominant peaks at 2θ of about 32.4°, 39.9°, 46.4°, 57.8°, 67.8° and 77.2°, which represent the indices of (110), (111), (200), (211), (220), and (310) planes, respectively (Khunrattanaphon *et al.*, 2011), conform to the crystalline structure of $SrTiO_3$. Therefore, the incorporation of SiO_2 and ZrO_2 with the investigated contents did not significantly affect the crystalline structure.

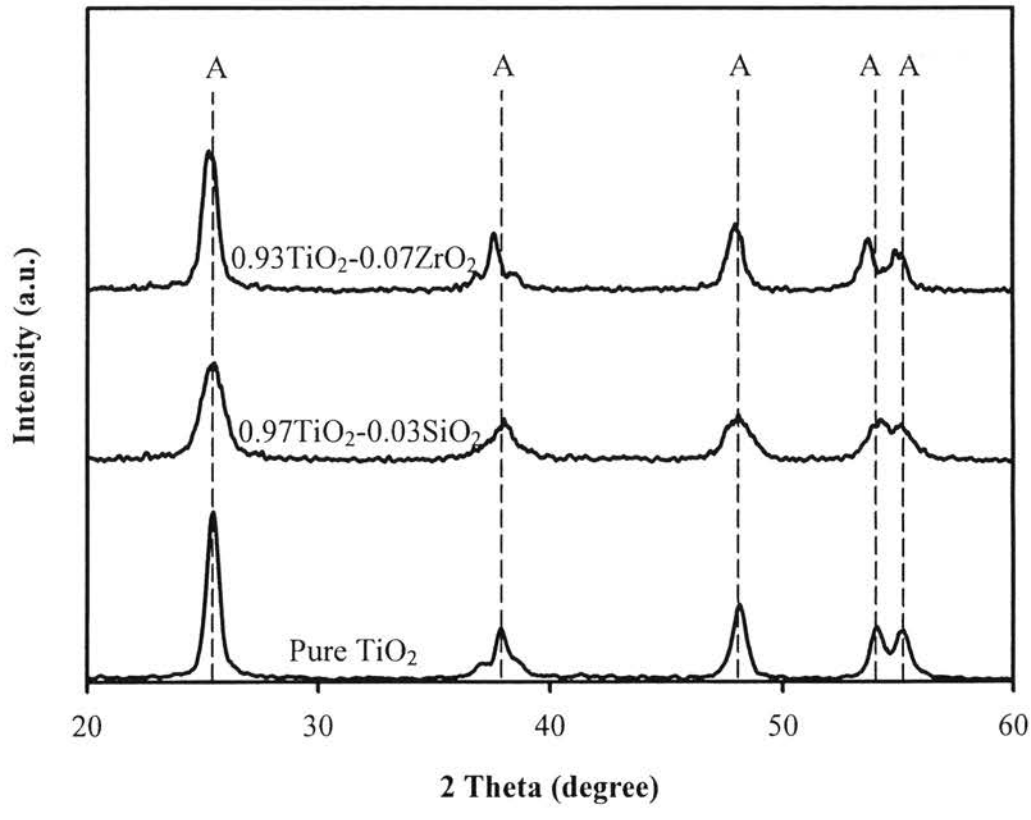

Figure 4.8 XRD patterns of the synthesized mesoporous-assembled pure TiO_2, $0.97TiO_2$-$0.03SiO_2$, and $0.93TiO_2$-$0.07ZrO_2$ photocatalysts calcined at 500 °C (A = Anatase TiO_2).

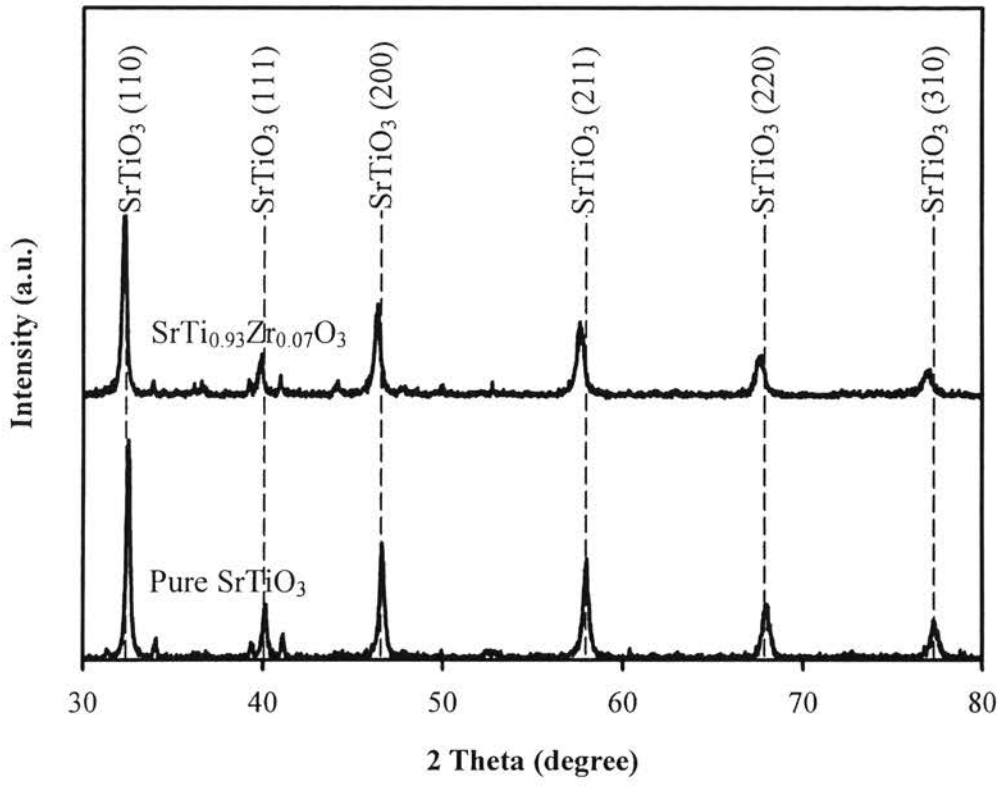

Figure 4.9 XRD patterns of the synthesized mesoporous-assembled pure $SrTiO_3$ and $SrTi_{0.93}Zr_{0.07}O_3$ photocatalysts calcined at 700 °C.

The crystallite size of the photocatalysts is calculated from the line broadening of the most preferentially oriented diffraction peak of each crystalline phase according to the Scherrer equation (Cullity, 1978) (Eq.4.1):

$$L = \frac{k\lambda}{\beta \cos(\theta)} \tag{4.1}$$

where L is the crystallite size, k is the Scherrer constant usually taken as 0.89, λ is the wavelength of the X-ray radiation (0.15418 nm for Cu Kα), β is the full width at half maximum (FWHM) of the diffraction peak measured at 2θ, and θ is the diffraction angle. The crystallite sizes of the synthesized mesoporous-assembled pure TiO_2 $0.97TiO_2$-$0.03SiO_2$, $0.93TiO_2$-$0.07ZrO_2$, pure $SrTiO_3$ and $SrTi_{0.93}Zr_{0.07}O_3$ photocatalysts are summarized in Table 4.5. The incorporation of SiO_2 and ZrO_2 led

to a decrease in crystallite size since the added SiO_2 and ZrO_2 play a positive role in retarding the photocatalysts' grain growth (Rungjareontawon, 2011).

Table 4.5 Crystallite size results of the synthesized mesoporous-assembled pure TiO_2 $0.97TiO_2$-$0.03SiO_2$, $0.93TiO_2$-$0.07ZrO_2$, pure $SrTiO_3$ and $SrTi_{0.93}Zr_{0.07}O_3$ photocatalysts.

Photocatalyst	Calcination temperature (°C)	Phase from XRD pattern	Crystallite size (nm)
Pure TiO_2	500	Anatase	14.66
$0.97TiO_2$-$0.03SiO_2$	500	Anatase	6.97
$0.93TiO_2$-$0.07ZrO_2$	500	Anatase	10.11
Pure $SrTiO_3$	700	Cubic	26.30
$SrTi_{0.93}Zr_{0.07}O_3$	700	Cubic	24.99

Figures 4.10-4.11 shows the XRD patterns of the synthesized bimetallic Pt-Ag-loaded mesoporous-assembled $0.97TiO_2$-$0.03SiO_2$ and $0.93TiO_2$-$0.07ZrO_2$ photocatalysts calcined at 500 °C. All the diffraction peaks correspond to the crystalline structure of the anatase TiO_2. The peaks observed at 2θ of 32.3° and 46.2 represent the indices of Ag and Pt phases, respectively (Ashkarrn *et al.*, 2011). However, the peak intensities were quite week possibly due to the low contents of both metals. In case of the synthesized bimetallic Pt-Ag-loaded mesoporous-assembled $SrTi_{0.93}Zr_{0.07}O_3$ photocatalysts calcined at 700 °C (Figure 4.12), it was found that all the diffraction peaks correspond to the crystalline structure of the cubic $SrTiO_3$. The presence of the Ag and Pt phases was not clearly observed in the XRD

patterns, as shown in Figure 4.12. From Table 4.6, it can be concluded that the bimetallic Pt-Ag loadings slightly affect the crystallite size of all samples.

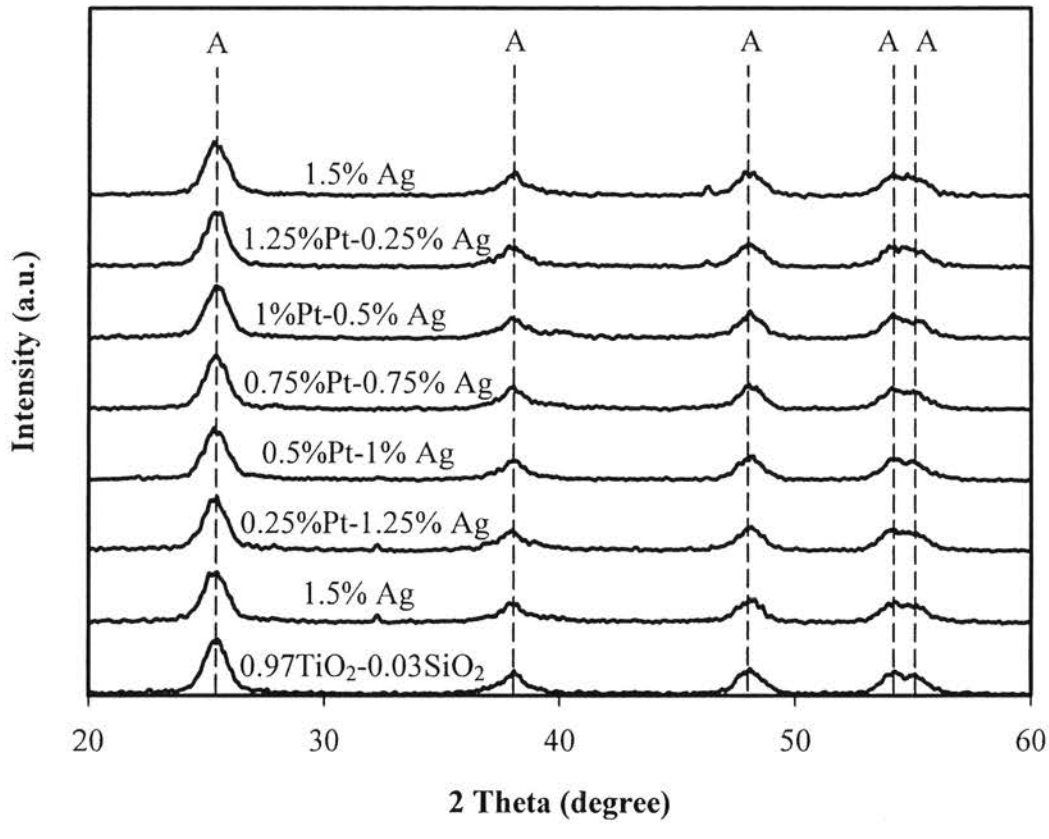

Figure 4.10 XRD patterns of the synthesized bimetallic Pt-Ag-loaded mesoporous-assembled $0.97TiO_2$-$0.03SiO_2$ photocatalysts calcined at 500 °C, (A = Anatase TiO_2)

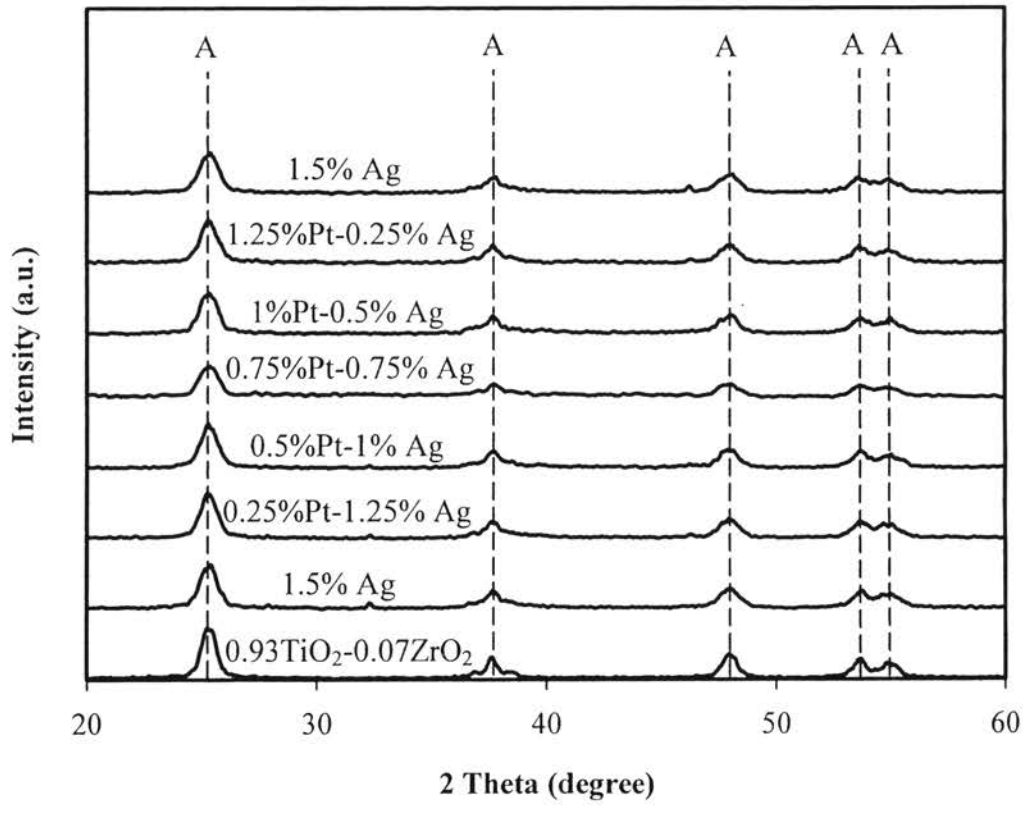

Figure 4.11 XRD patterns of the synthesized bimetallic Pt-Ag-loaded mesoporous-assembled $0.93TiO_2$-$0.07ZrO_2$ photocatalysts calcined at 500 °C (A = Anatase TiO_2).

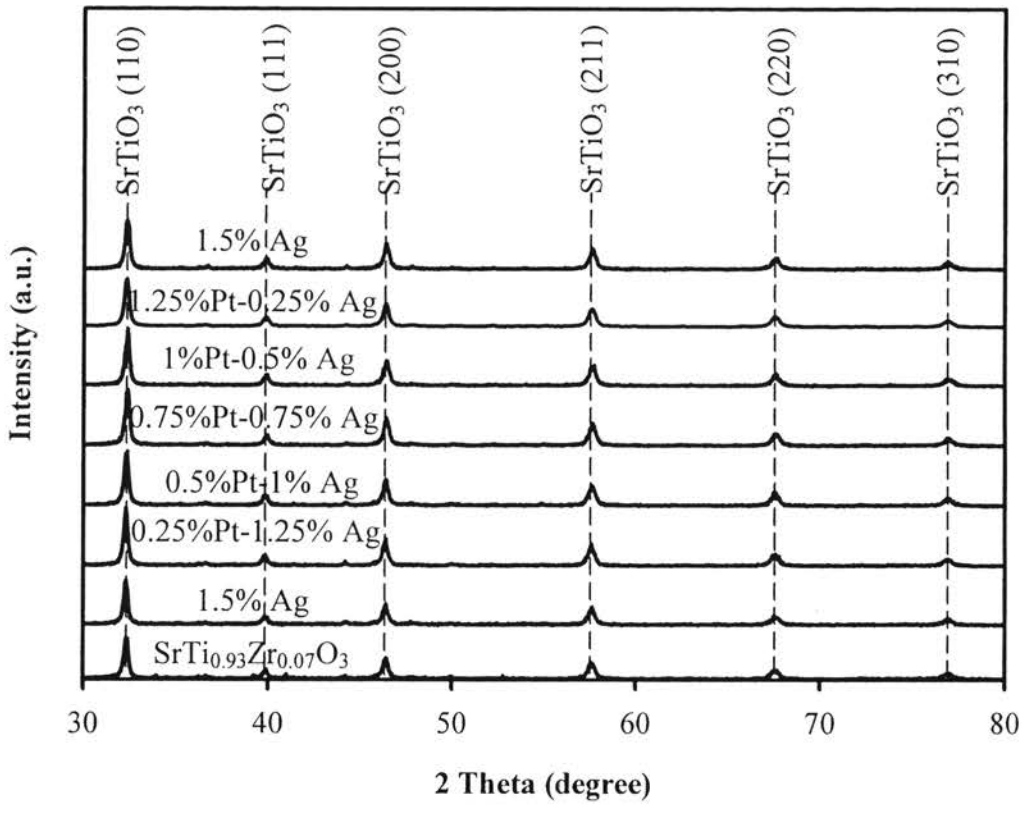

Figure 4.12 XRD patterns of the synthesized bimetallic Pt-Ag-loaded mesoporous-assembled $SrTi_{0.93}Zr_{0.07}O_3$ photocatalysts calcined at 700 °C.

Table 4.6 Crystallite size results of the synthesized bimetallic Pt-Ag-loaded mesoporous-assembled $0.97TiO_2$-$0.03SiO_2$, $0.93TiO_2$-$0.07ZrO_2$, and $SrTi_{0.93}Zr_{0.07}O_3$ photocatalysts calcined at 500 °C, 500 °C, and 700 °C, respectively

Pt loading (wt.%)	Ag loading (wt.%)	$0.97TiO_2$-$0.03SiO_2$	$0.93TiO_2$-$0.07ZrO_2$	$SrTi_{0.93}Zr_{0.07}O_3$
		Anatase (101) crystallite size (nm)	Anatase (101) crystallite size (nm)	Cubic (110) crystallite size (nm)
0	0	6.96	10.11	24.99
1.5	0	6.79	8.69	24.59
1.25	0.25	6.85	8.99	21.43
1	0.5	6.61	9.22	22.17
0.75	0.75	6.78	9.12	24.58
0.5	1	6.56	7.96	25.24
0.25	1.25	6.88	7.80	24.75
0	1.5	7.04	9.29	24.91

4.1.4 UV-Visible Spectroscopy Results

UV-visible spectroscopy was used to determine light absorption ability of the synthesized mesoporous-assembled $0.97TiO_2$-$0.03SiO_2$, $0.93TiO_2$-$0.07ZrO_2$, and $SrTi_{0.93}Zr_{0.07}O_3$ photocatalysts without and with Pt-Ag loadings. Figure 4.13 shows the UV-visible spectra of the pure TiO_2, $0.97TiO_2$-$0.03SiO_2$, and $0.93TiO_2$-$0.07ZrO_2$ photocatalysts calcined at 500 °C. It can be clearly observed that the absorption band of the synthesized mesoporous-assembled $0.97TiO_2$-$0.03SiO_2$ and $0.93TiO_2$-$0.07ZrO_2$ photocatalysts is mainly in the UV light region in the range of low wavelength up to 400 nm. Figure 4.14 shows the UV-visible spectra of the

mesoporous-assembled $SrTiO_3$ and $SrTi_{0.93}Zr_{0.07}O_3$ photocatalysts calcined at 700 °C. It was also found that the main absorption band is in the UV light region in the range of 200-400 nm. The band gap energy (E_g, eV) is determined by extrapolating the absorption onset of the rising part to x-axis (λ_g, nm) of the plots and calculating by following equation (4.2)

$$E_g = 1240 / \lambda_g \quad (4.2)$$

where λ_g is the onset absorption wavelength (nm) of the exciting light. The results of absorption onset wavelength and corresponding ban gap energy of the photocatalysts obtained from the UV-visible spectra are summarized in Table 4.7. With SiO_2 incorporation, the band gap energy increased from 3.20 eV (λ_g = 387 nm) for the pure TiO_2 to 3.26 eV (λ_g = 380 nm) for the $0.97TiO_2$-$0.03SiO_2$. In case of the $0.93TiO_2$-$0.07ZrO_2$, it was found that the band gap energy increased to 3.22 eV (λ_g = 385). The band gap energy of $SrTiO_3$ is 3.12 eV (λ_g = 398 nm), while it was increased to 3.20 eV (λ_g = 387) for the $SrTi_{0.93}Zr_{0.07}O_3$. The shift of the absorption onset edge with the incorporation of SiO_2 and ZrO_2 can be attributed to quantum-size effect for smaller crystallites (Onsuratoom *et al.,* 2011). Table 4.8 shows the comparative results of absorption onset wavelength and corresponding band gap energy of the mesoporous-assembled $0.97TiO_2$-$0.03SiO_2$, $0.93TiO_2$-$0.07ZrO_2$, and $SrTi_{0.93}Zr_{0.07}O_3$ photocatalysts with bimetallic Pt-Ag loadings. It can be seen that the band gap energy of the bimetallic Pt-Ag-loaded $0.93TiO_2$-$0.07ZrO_2$ photocatalysts increased when compared to the unloaded photocatalyst due to a decrease in the absorption onset wavelength, whereas the bimetallic Pt-Ag-loaded $0.97TiO_2$-$0.03SiO_2$ and $SrTi_{0.93}Zr_{0.07}O_3$ photocatalysts possessed the band gap energy lower than that of the unloaded photocatalysts. The results of UV-visible spectra of the mesoporous-assembled $0.97TiO_2$-$0.03SiO_2$, $0.93TiO_2$-$0.07ZrO_2$, and $SrTi_{0.93}Zr_{0.07}O_3$ photocatalysts without and with bimetallic Pt-Ag loadings are depicted in Figure 4.15-4.17. The results show that the band gap energies of the 1.25 wt.% Pt-0.25 wt.% Ag-loaded $0.97TiO_2$-$0.03SiO_2$ and 1.25 wt.% Pt-0.25 wt.% Ag-loaded $SrTi_{0.93}Zr_{0.07}O_3$ are 3.16 eV (λ_g = 393 nm) and 3.15 eV (λ_g = 394 nm), respectively, which are lower than the band gap energies of the $0.97TiO_2$-$0.03SiO_2$ and $SrTi_{0.93}Zr_{0.07}O_3$, respectively. It can be implied that the bimetallic Pt-Ag loaded on

photocatalyst surface created the Schottky barrier, resulting in a decrease in the band gap energy (Onsuratoom *et al.*, 2011). It can also be seen that the bimetallic Pt-Ag-loaded samples showed more visible light absorption ability than the unloaded samples. In order to prove that Eosin Y (E.Y.) responds in the visible-light region, its UV-visible spectrum is shown in Figure 4.18. It is clearly seen that the E.Y. can mainly absorb the visible light with the maximum absorption at 516 nm. Therefore, the E.Y. sensitizer can be activated by the visible-light for the sensitized photocatalytic hydrogen production (Rungjareontawon, 2011).

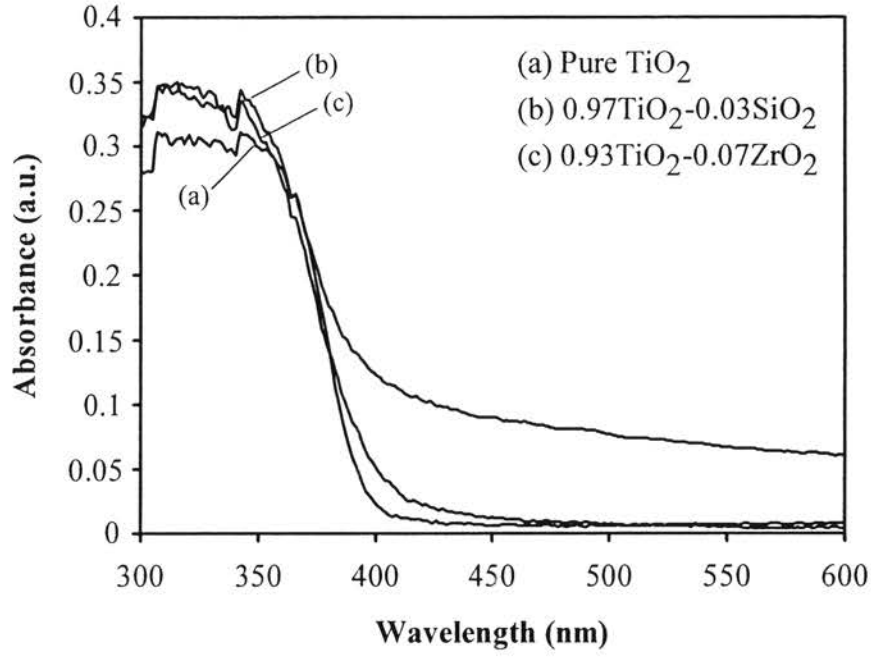

Figure 4.13 UV-visible spectra of the synthesized mesoporous-assembled photocatalysts calcined at 500 °C: (a) pure TiO_2, and (b) $0.97TiO_2$-$0.03SiO_2$, and (c) $0.93TiO_2$-$0.07ZrO_2$.

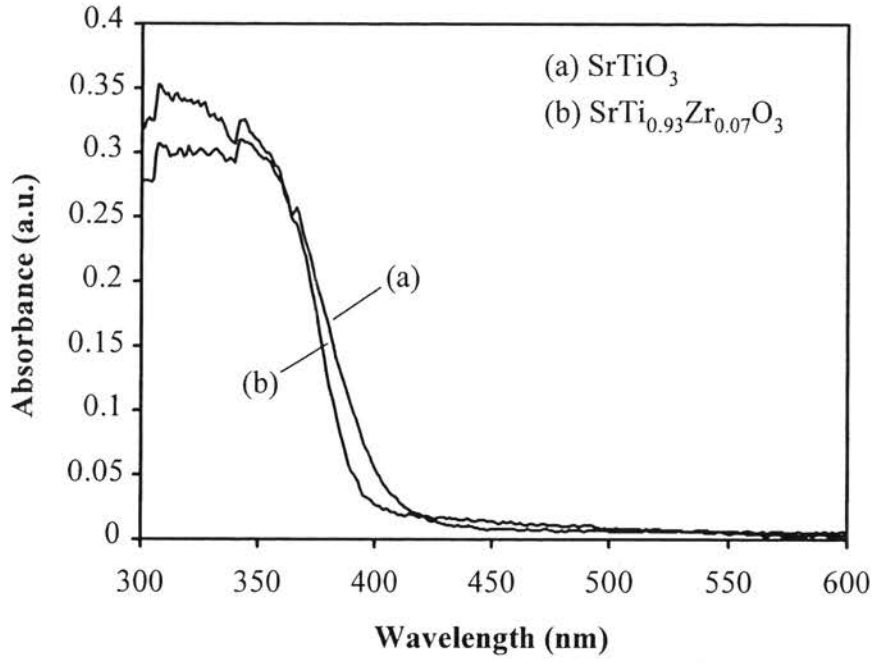

Figure 4.14 UV-visible spectra of the synthesized mesoporous-assembled photocatalysts calcined at 700 °C: (a) $SrTiO_3$ and (b) $SrTi_{0.93}Zr_{0.07}O_3$.

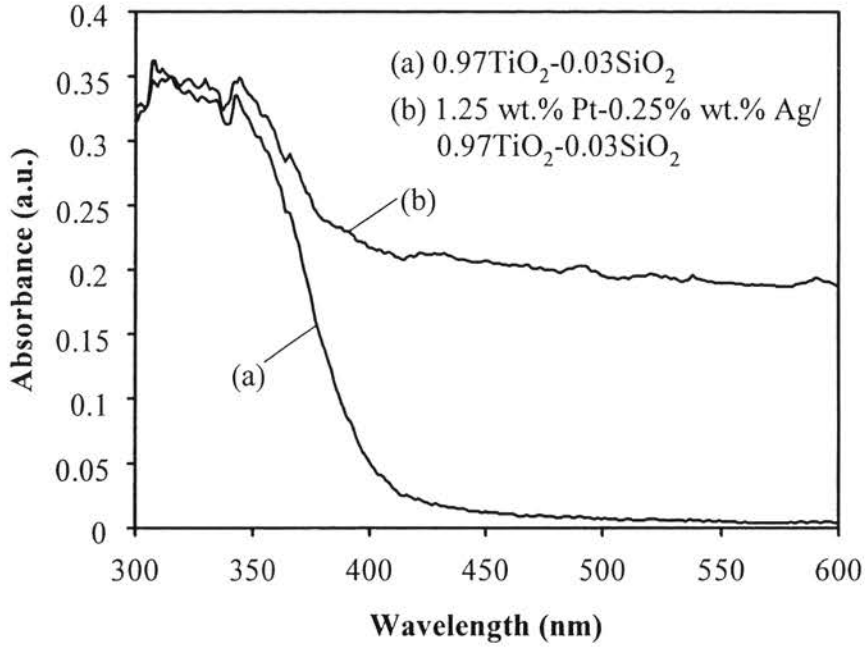

Figure 4.15 UV-visible spectra of the synthesized mesoporous-assembled photocatalysts calcined at 500 °C: (a) $0.97TiO_2$-$0.03SiO_2$ and (b) 1.25 wt.% Pt-0.25 wt.% Ag-loaded $0.97TiO_2$-$0.03SiO_2$.

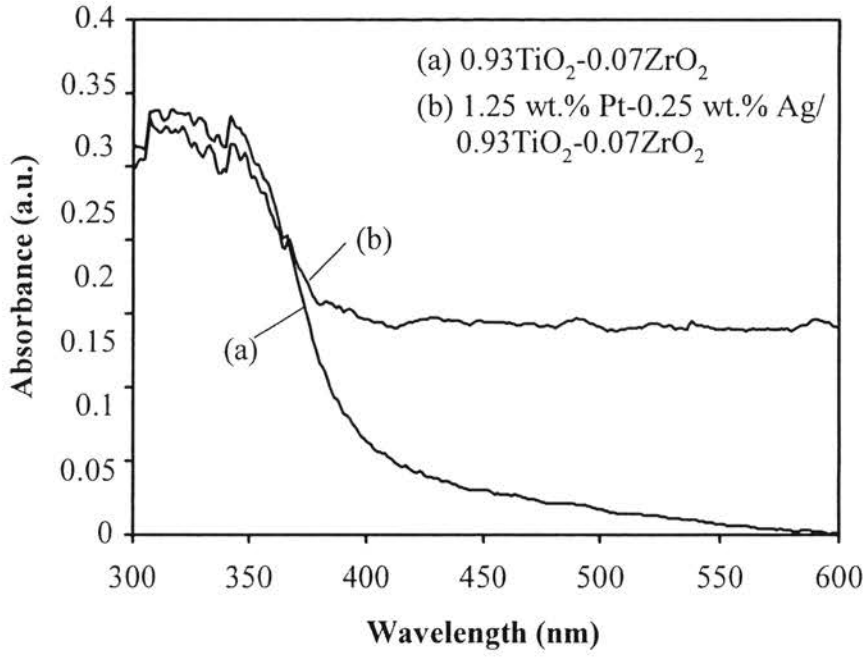

Figure 4.16 UV-visible spectra of the synthesized mesoporous-assembled photocatalysts calcined at 500 °C: (a) $0.93TiO_2$-$0.07ZrO_2$ and (b) 1.25 wt.% Pt-0.25 wt.% Ag-loaded $0.93TiO_2$-$0.07ZrO_2$.

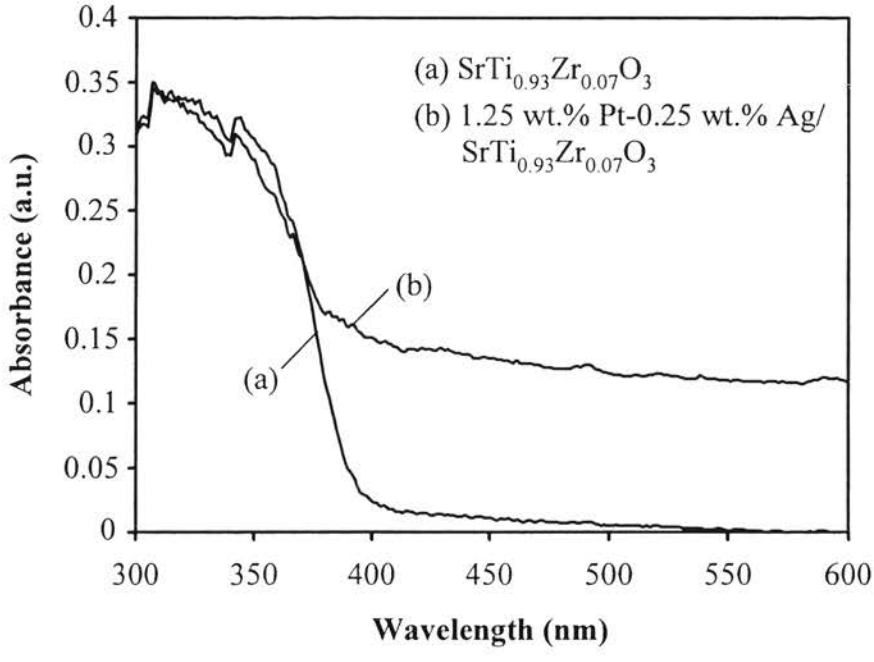

Figure 4.17 UV-visible spectra of the synthesized mesoporous-assembled photocatalysts calcined at 700 °C: (a) $SrTi_{0.93}Zr_{0.07}O_3$ and (b) 1.25 wt.% Pt-0.25 wt.% Ag-loaded $SrTi_{0.93}Zr_{0.07}O_3$.

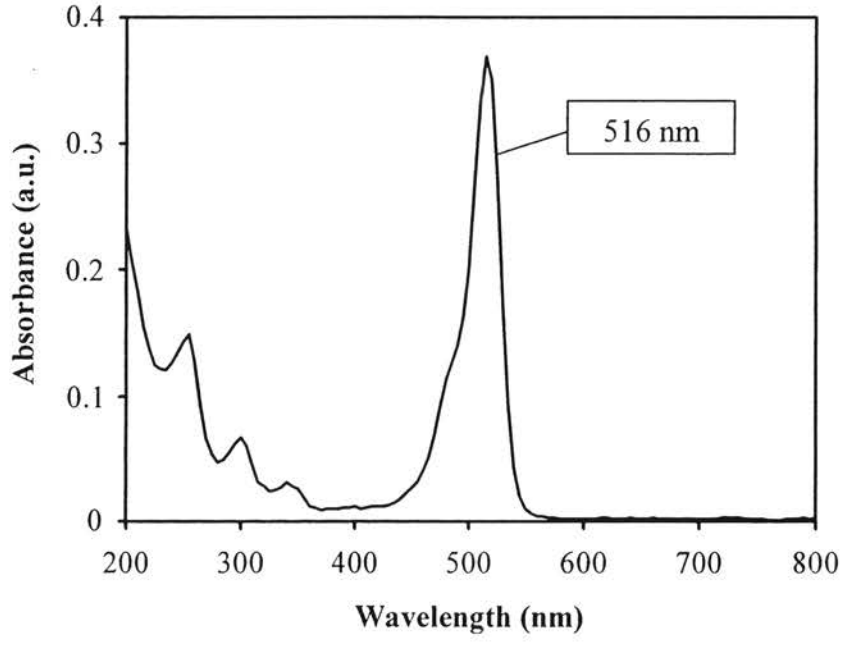

Figure 4.18 UV-visible spectrum of Eosin Y solution.

Table 4.7 Absorption onset wavelength and ban gap energy results of the synthesized mesoporous-assembled $0.97TiO_2$-$0.03SiO_2$, $0.93TiO_2$-$0.07ZrO_2$, and $SrTi_{0.93}Zr_{0.07}O_3$ photocatalysts

Photocatalyst	Calcination temperature (°C)	Absorption onset wavelength, λ_g (nm)	Band gap energy (eV)
Pure TiO_2	500	387	3.20
$0.97TiO_2$-$0.03SiO_2$	500	380	3.26
$0.93TiO_2$-$0.07ZrO_2$	500	385	3.22
$SrTiO_3$	700	398	3.12
$SrTi_{0.93}Zr_{0.07}O_3$	700	387	3.20

Table 4.8 Absorption onset wavelength and ban gap energy results of the synthesized mesoporous-assembled $0.97TiO_2$-$0.03SiO_2$, $0.93TiO_2$-$0.07ZrO_2$, and $SrTi_{0.93}Zr_{0.07}O_3$ photocatalysts with bimetallic Pt-Ag loadings

Photocatalyst	Calcination temperature (°C)	Pt loading (wt.%)	Ag loading (wt.%)	Absorption onset wavelength, λ_g (nm)	Band gap energy (eV)
$0.97TiO_2$-$0.03SiO_2$	500	1.5	0	387	3.20
		1.25	0.25	393	3.16
		1	0.5	387	3.20
		0.75	0.75	389	3.19
		0.5	1	389	3.19
		0.25	1.25	387	3.20
		0	1.5	389	3.19
$0.93TiO_2$-$0.07ZrO_2$	500	1.5	0	383	3.24
		1.25	0.25	387	3.20
		1	0.5	383	3.24
		0.75	0.75	381	3.25
		0.5	1	383	3.24
		0.25	1.25	383	3.24
		0	1.5	381	3.25
$SrTi_{0.93}Zr_{0.07}O_3$	700	1.5	0	389	3.19
		1.25	0.25	394	3.15
		1	0.5	389	3.19
		0.75	0.75	389	3.19
		0.5	1	391	3.17
		0.25	1.25	391	3.17
		0	1.5	391	3.17

4.1.5 SEM-EDX Results

The morphology of the photocatalysts was observed by the SEM analysis. Figures 4.19-4.21 depict the SEM images of the mesoporous-assembled $0.97TiO_2$-$0.03SiO_2$, $0.93TiO_2$-$0.07ZrO_2$, and $SrTi_{0.93}Zr_{0.07}O_3$ photocatalysts without and with bimetallic Pt-Ag loadings. The images clearly show the presence of agglomerated clusters formed by an aggregation of several uniform-sized photocatalyst nanoparticles. Therefore, the nanoparticle aggregation plausibly led to the formation of mesoporous-assembled structure in the synthesized photocatalysts. The elemental distributions on the 1.25 wt.% Pt-0.25 wt.% Ag-loaded $0.97TiO_2$-$0.03SiO_2$, 1.25 wt.% Pt-0.25 wt.% Ag-loaded $0.93TiO_2$-$0.07ZrO_2$, and 1.25 wt.% Pt-0.25 wt.% Ag-loaded $SrTi_{0.93}Zr_{0.07}O_3$ photocatalysts were also examined by using the EDX analysis, as shown in Figures 4.22-4.24, respectively. The existence of dots in the elemental mappings of all the investigated species reveals that all the elements in the bimetallic Pt-Ag-loaded $0.97TiO_2$-$0.03SiO_2$, $0.93TiO_2$-$0.07ZrO_2$, and $SrTi_{0.93}Zr_{0.07}O_3$ were well dispersed throughout the bulk photocatalysts. These results confirm the high dispersion state of the deposited Pt-Au particles on the photocatalysts prepared by the PCD method.

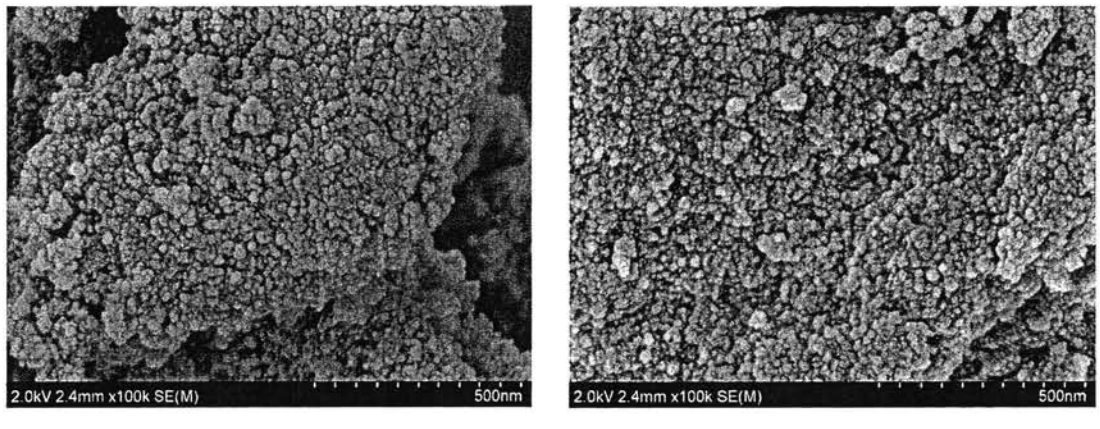

(a) (b)

Figure 4.19 SEM images of the synthesized mesoporous-assembled photocatalysts calcined at 500 °C: (a) $0.97TiO_2$-$0.03SiO_2$ and (b) 1.25 wt.% Pt-0.25 wt.% Ag-loaded $0.97TiO_2$-$0.03SiO_2$.

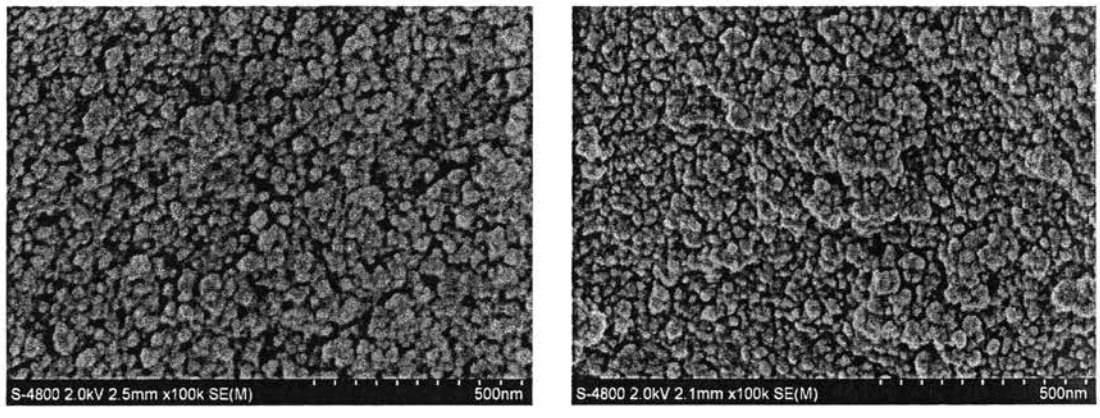

(a) (b)

Figure 4.20 SEM images of the synthesized mesoporous-assembled photocatalysts calcined at 500 °C: (a) $0.93TiO_2$-$0.07ZrO_2$ and (b) 1.25 wt.% Pt-0.25 wt.% Ag-loaded $0.93TiO_2$-$0.07ZrO_2$.

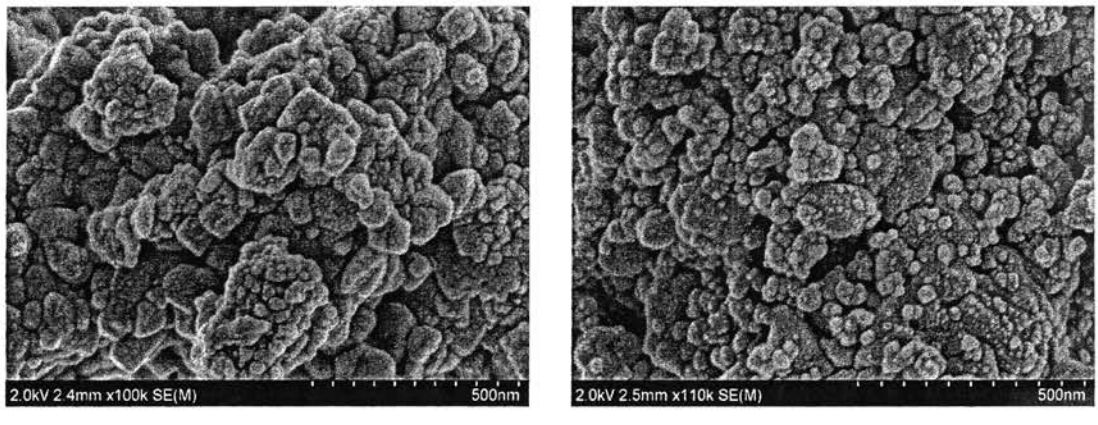

(a) (b)

Figure 4.21 SEM images of the synthesized mesoporous-assembled photocatalysts calcined at 700 °C: (a) $SrTi_{0.93}Zr_{0.07}O_3$ and (b) 1.25 wt.% Pt-0.25 wt.% Ag-loaded $SrTi_{0.93}Zr_{0.07}O_3$.

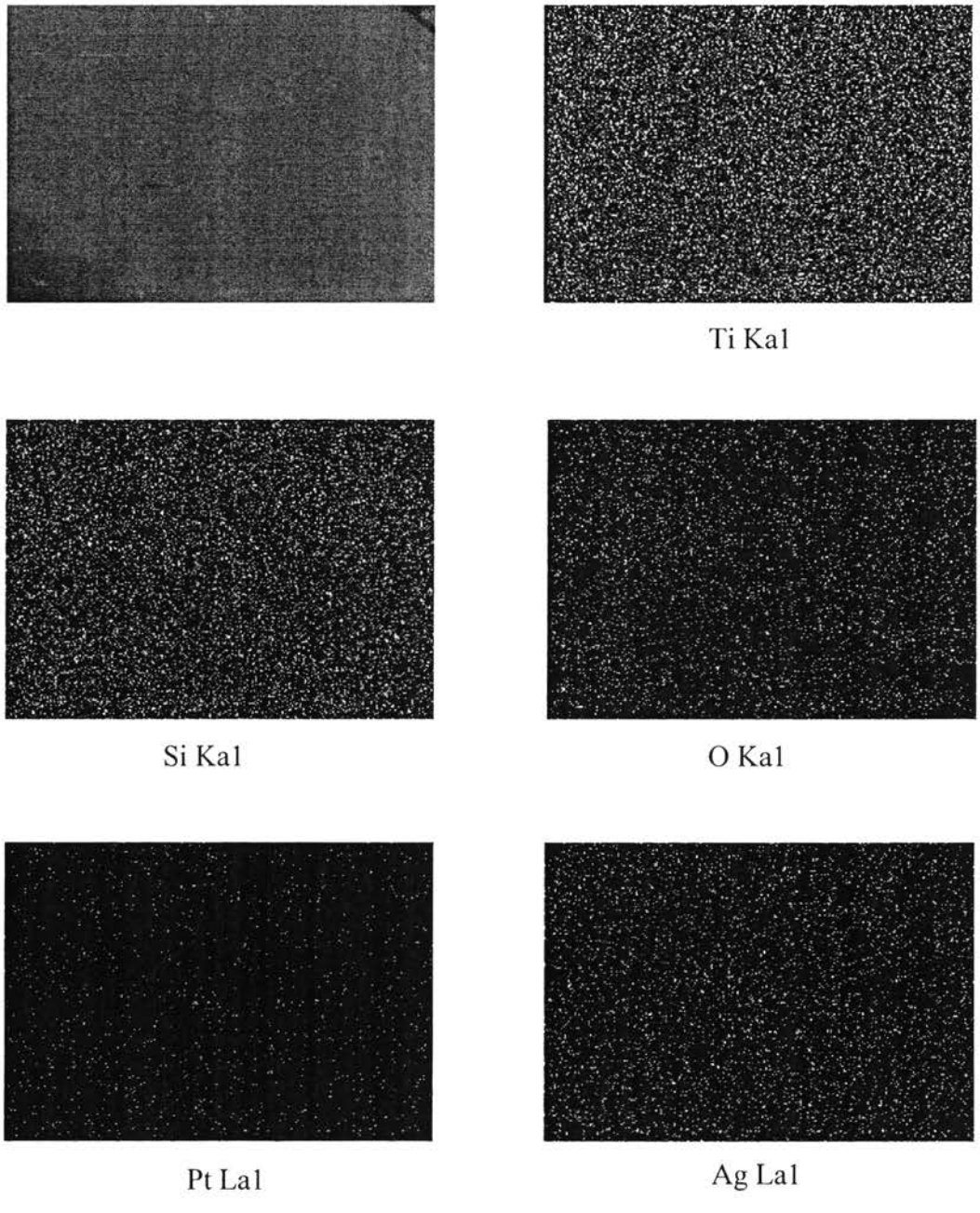

Figure 4.22 SEM image and EDX area mappings of the synthesized 1.25 wt.% Pt-0.25 wt.% Ag-loaded mesoporous-assembled $0.97TiO_2$-$0.03SiO_2$ photocatalyst calcined at 500 °C.

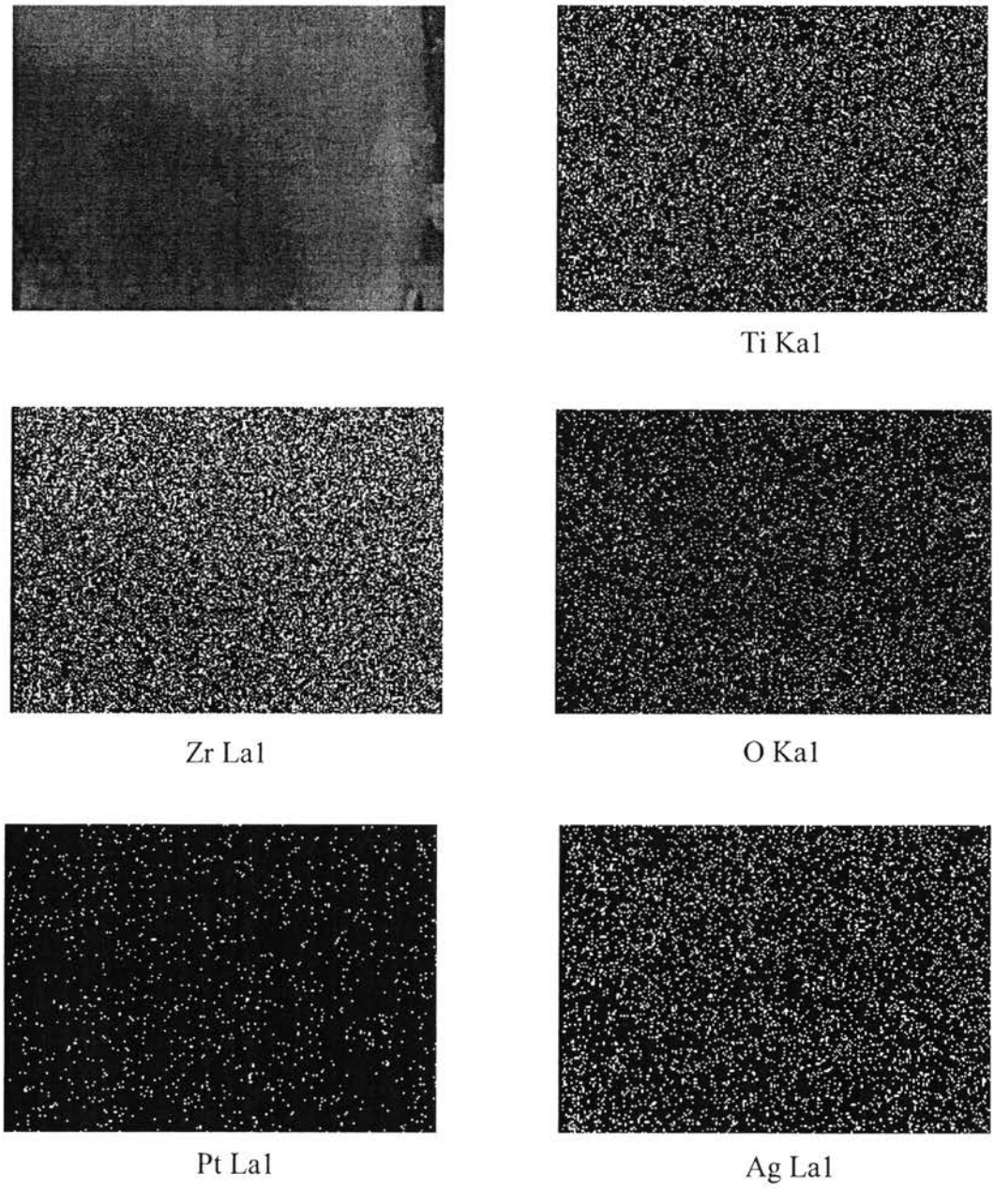

Figure 4.23 SEM image and EDX area mappings of the synthesized 1.25 wt.% Pt-0.25 wt.% Ag-loaded mesoporous-assembled $0.93TiO_2$-$0.07ZrO_2$ photocatalyst calcined at 500 °C.

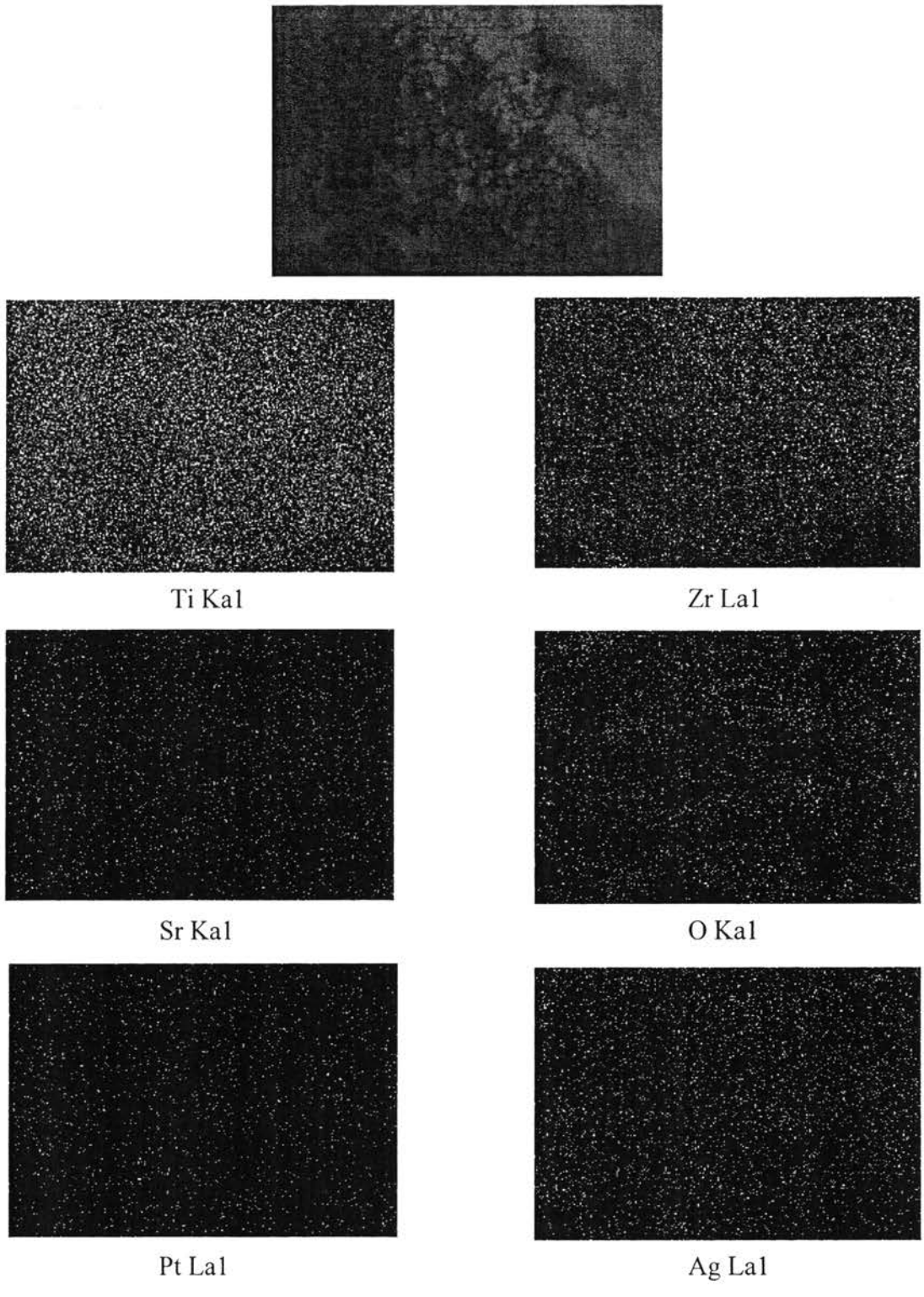

Figure 4.24 SEM image and EDX area mappings of the synthesized 1.25 wt.% Pt-0.25 wt.% Ag-loaded mesoporous-assembled $SrTi_{0.93}Zr_{0.07}O_3$ photocatalyst calcined at 700 °C.

4.1.6 TEM-EDX Results

The morphology of all the photocatalysts was also investigated by the TEM analysis. Figure 4.25 shows the exemplified TEM images of the synthesized mesoporous-assembled pure TiO_2, $0.97TiO_2$-$0.03SiO_2$, and $0.93TiO_2$-$0.07ZrO_2$ photocatalysts calcined at 500 °C. The aggregated photocatalyst nanoparticles can be clearly observed. The average particle sizes of pure TiO_2, $0.97TiO_2$-$0.03SiO_2$, and $0.93TiO_2$-$0.07ZrO_2$ photocatalysts were in the range 10-16, 5-10, and 8-15 nm, respectively. Figure 4.26 illustrates the TEM images of the synthesized mesoporous-assembled pure $SrTiO_3$ and $SrTi_{0.93}Zr_{0.07}O_3$ photocatalysts calcined at 700 °C. The average particle sizes were in the range of 20-38 nm for the pure $SrTiO_3$ and 20-33 nm for the $SrTi_{0.93}Zr_{0.07}O_3$. The decrease in particle sizes of the photocatalysts may be due to the thermal stability and the resistance to sintering from the incorporated SiO_2 and ZrO_2. Figures 4.27-4.29 show the TEM images and EDX point mappings of the synthesized bimetallic 1.25 wt.% Pt-0.25 wt.% Ag-loaded $0.97TiO_2$-$0.03SiO_2$, 1.25 wt.% Pt-0.25 wt.% Ag-loaded $0.93TiO_2$-$0.07ZrO_2$, and 1.25 wt.% Pt-0.25 wt.% Ag-loaded $SrTi_{0.93}Zr_{0.07}O_3$ photocatalysts, respectively. The Pt and Ag nanoparticles can be clearly seen as dark patches due to their high electron density, as confirmed by the EDX mappings.

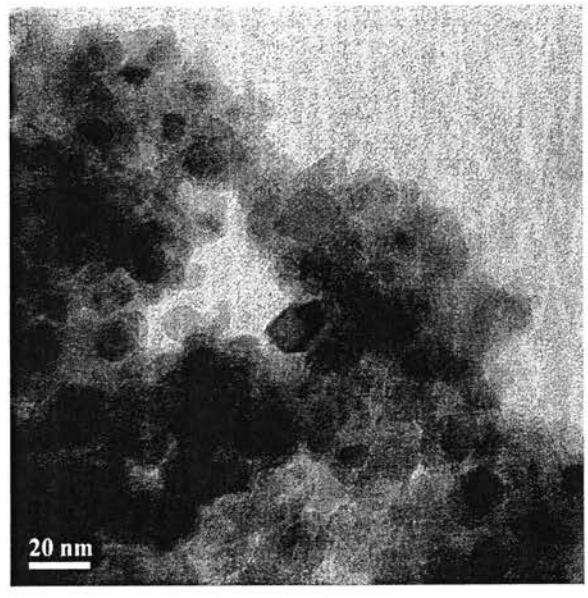

(a)

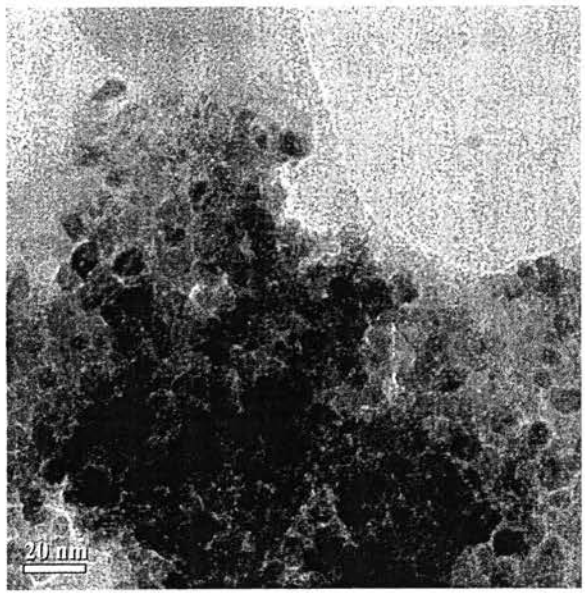

(b)

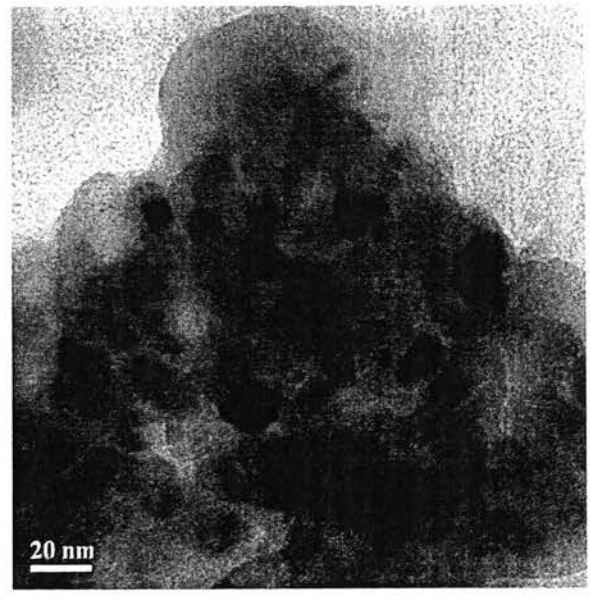

(c)

Figure 4.25 TEM images of synthesized mesoporous-assembled photocatalysts calcined at 500 °C: (a) pure TiO_2, (b) $0.97TiO_2$-$0.03SiO_2$, and (c) $0.93TiO_2$-$0.07ZrO_2$

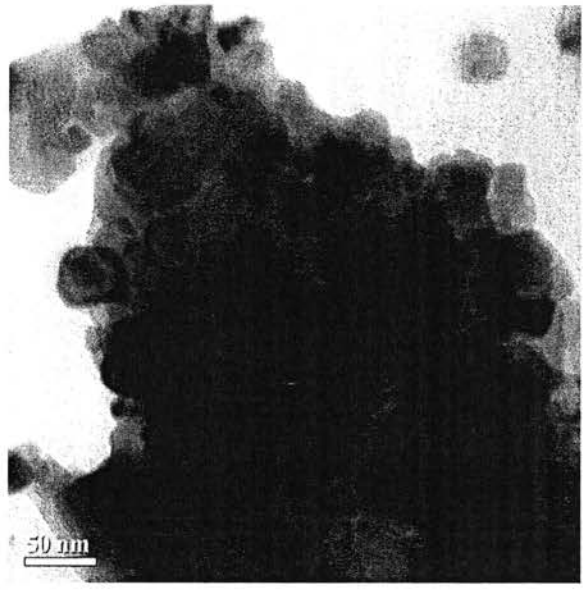

(a)

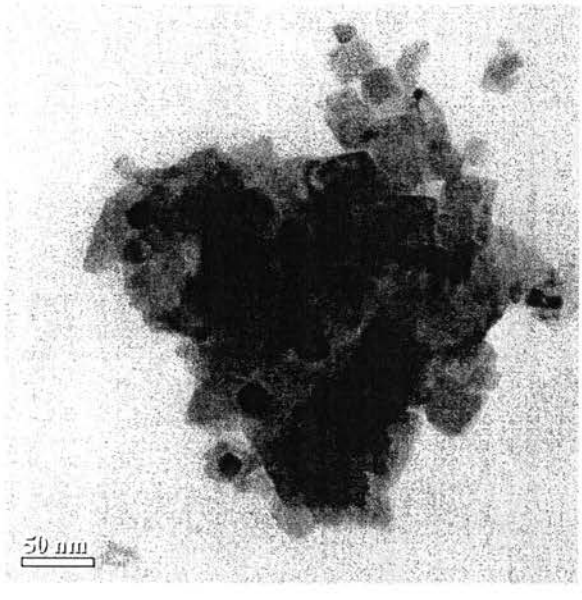

(b)

Figure 4.26 TEM images of synthesized mesoporous-assembled photocatalysts calcined at 700 °C: (a) pure $SrTiO_3$ and (b) $SrTi_{0.93}Zr_{0.07}O_3$.

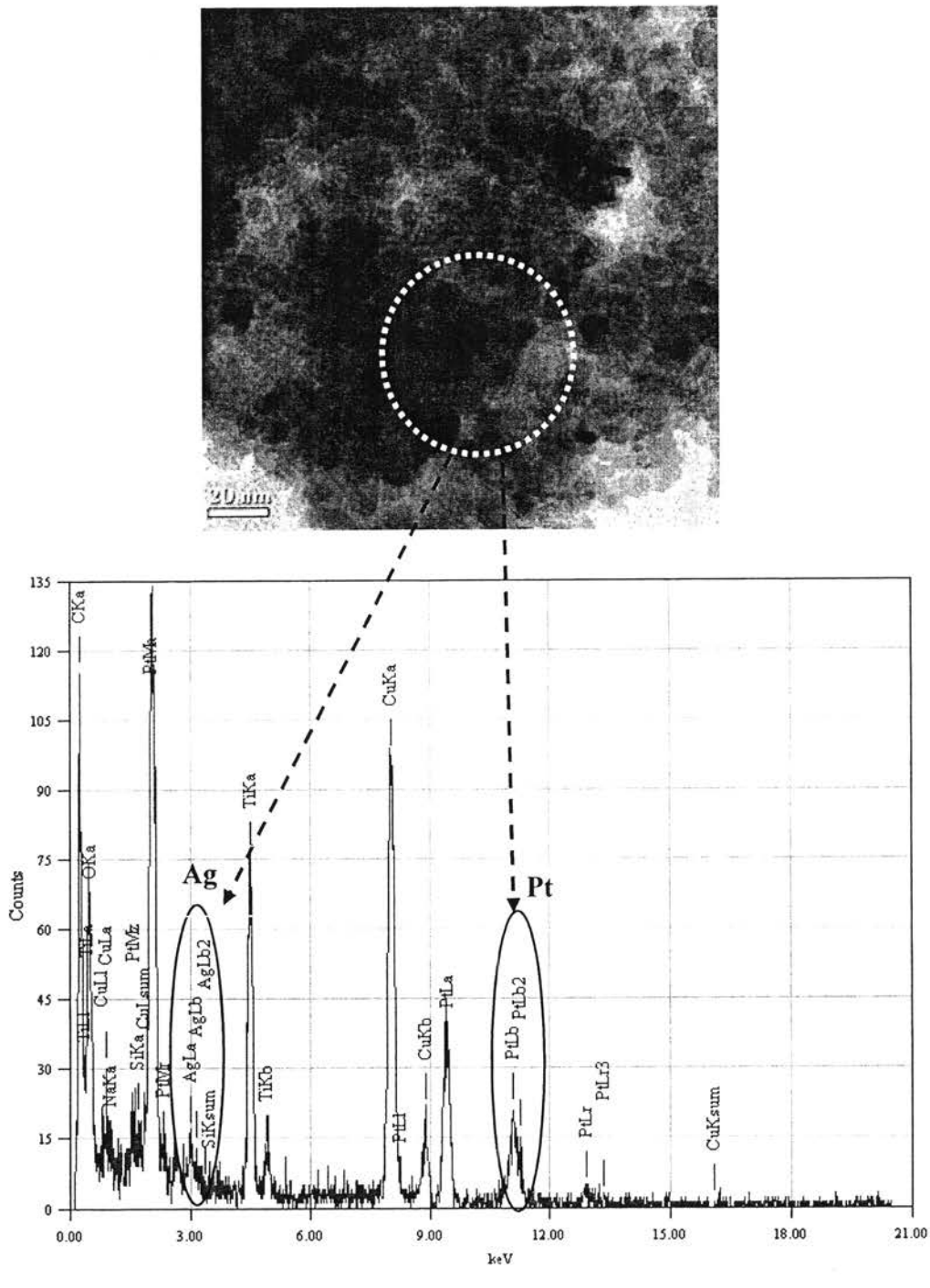

Figure 4.27 TEM image and EDX point mapping of the synthesized 1.25 wt.% Pt-0.25 wt.% Ag-loaded mesoporous-assembled $0.97TiO_2$-$0.03SiO_2$ photocatalyst calcined at 500 °C.

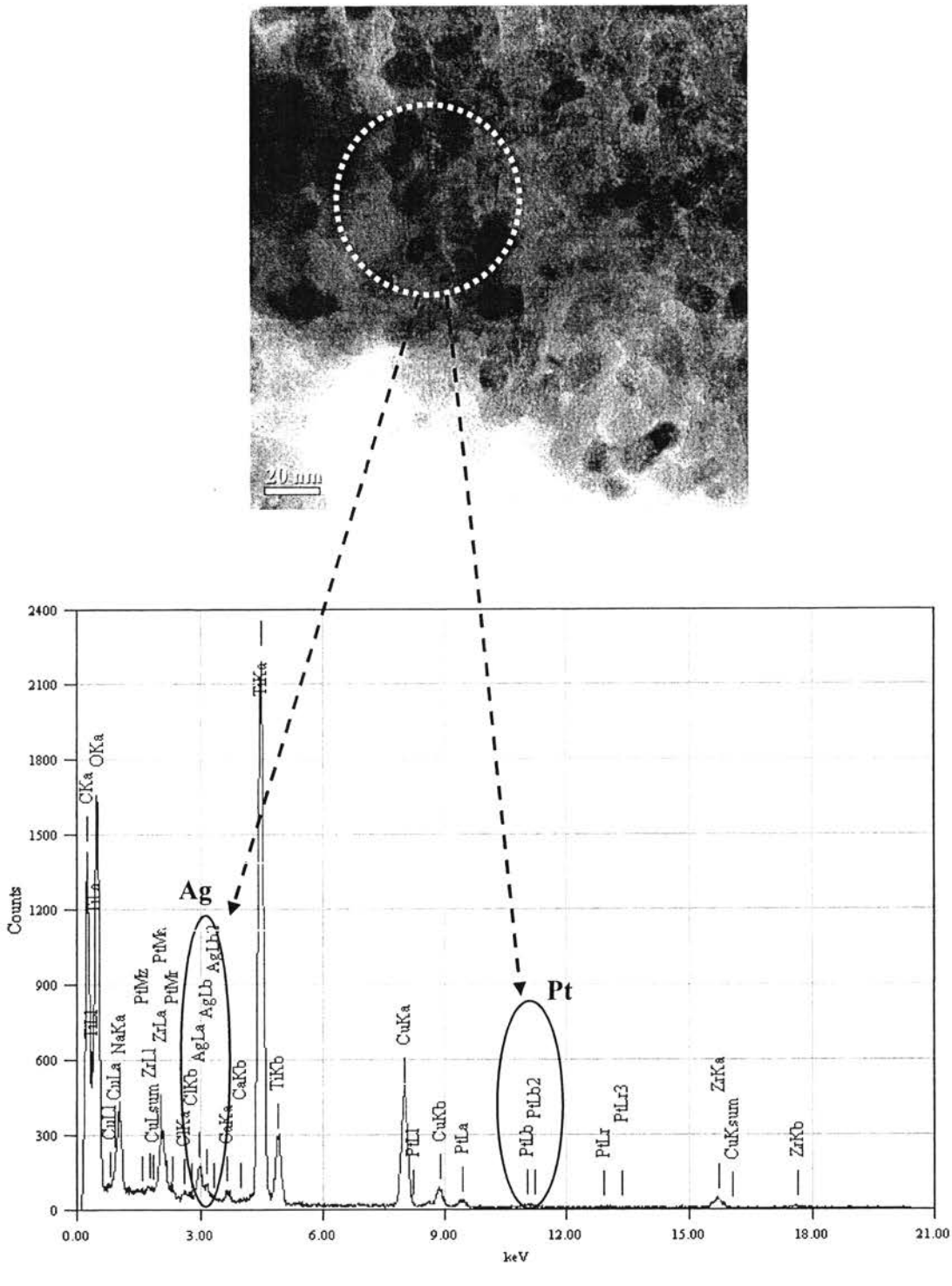

Figure 4.28 TEM image and EDX point mapping of the synthesized 1.25 wt.% Pt-0.25 wt.% Ag-loaded mesoporous-assembled $0.93TiO_2$-$0.07ZrO_2$ photocatalyst calcined at 500 °C.

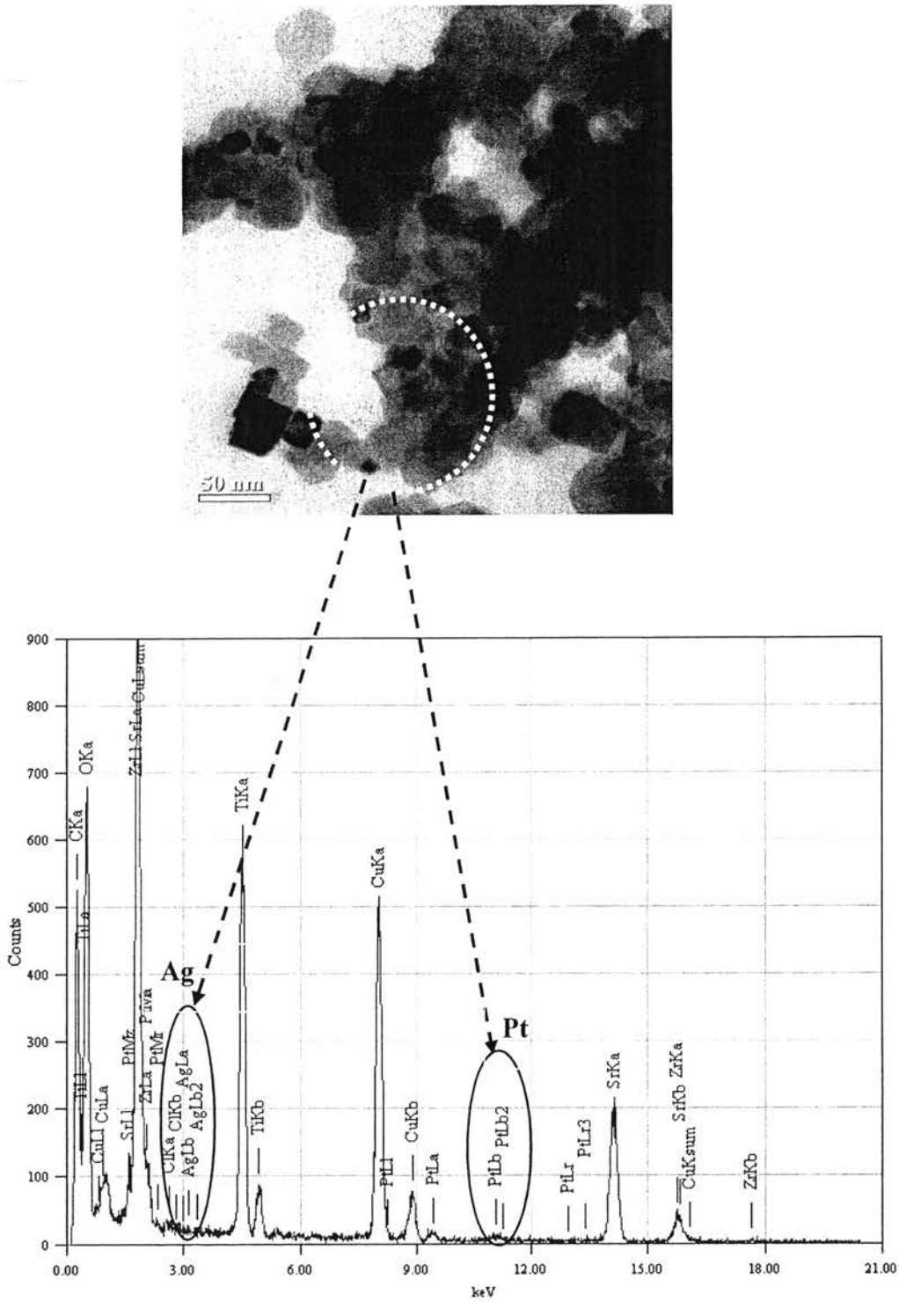

Figure 4.29 TEM image and EDX point mapping of the synthesized 1.25 wt.% Pt-0.25 wt.% Ag-loaded mesoporous-assembled $SrTi_{0.93}Zr_{0.07}O_3$ photocatalyst calcined at 700 °C.

4.1.7 Hydrogen Chemisorption Results

Hydrogen chemisorption analysis was used to determine the metal dispersion. The metal dispersion results of all the bimetallic Pt-Ag-loaded mesoporous-assembled photocatalysts are given in Table 4.9. It can be clearly seen that the metal dispersion increased with increasing Pt loading while decreasing Ag loading to reach a maximum value at the 1.25 wt.% Pt-0.25 wt.% Ag loading, and after that it decreased with further increasing Pt loading to be the monometallic 1.5 wt.% Pt, probably due to the Pt nanoparticle agglomeration at very high Pt loading (Rungjaroentawon, 2011). This also suggests that the increase in Ag loading negatively affects the hydrogen adsorption (Sung *et* al., 2011). The results show that for the three photocatalyst supports, the maximum metal dispersions of 56.24%, 51.50%, and 56.61% were observed for the 1.25 wt.% Pt-0.25 wt.% Ag-loaded $0.97TiO_2$-$0.03SiO_2$, the 1.25 wt.% Pt-0.25 wt.% Ag-loaded $0.93TiO_2$-$0.07ZrO_2$, and the 1.25 wt.% Pt-0.25 wt.% Ag-loaded $SrTi_{0.93}Zr_{0.07}O_3$, respectively. These results indicate that the PCD method employed for the metal loading is very efficient to be used to achieve the high metal dispersions under the investigated metal loading range.

Table 4.9 Metal dispersion results over the bimetallic Pt-Ag-loaded mesoporous-assembled $0.97TiO_2$-$0.03SiO_2$, $0.93TiO_2$-$0.07ZrO_2$, and $SrTi_{0.93}Zr_{0.07}O_3$ photocatalysts calcined at 500 °C, 500 °C, and 700 °C, respectively

Pt loading (wt.%)	Ag loading (wt.%)	Metal dispersion (%)		
		$0.97TiO_2$-$0.03SiO_2$	$0.93TiO_2$-$0.07ZrO_2$	$SrTi_{0.93}Zr_{0.07}O_3$
1.5	0	8.08	11.38	18.93
1.25	0.25	56.24	51.50	56.61
1	0.5	43.36	41.34	39.47
0.75	0.75	30.74	36.13	29.42
0.5	1	24.67	28.15	18.66
0.25	1.25	16.37	21.25	10.46
0	1.5	10.47	10.53	7.37

4.2 Photocatalytic Hydrogen Production Activity

In this photocatalytic reaction, the activity of the synthesized mesoporous-assembled $0.97TiO_2$-$0.03SiO_2$, $0.93TiO_2$-$0.07ZrO_2$, and $SrTi_{0.93}Zr_{0.07}O_3$ photocatalysts with different bimetallic Pt-Ag loadings were investigated for the sensitized hydrogen production from a diethanolamine (DEA) aqueous solution containing Eosin Y sensitizer (E.Y.) under visible light irradiation at room temperature. A 0.2 g of different types of all photocatalysts was suspended in 150 ml of 15 vol.% DEA aqueous solution (22.5 ml DEA and 127.5 ml distilled water) containing dissolved 0.1 mM E.Y and irradiated by visible light for 5 h.

4.2.1 Effect of Bimetallic Pt-Ag Loading

Noble metals are normally used to load on a photocatalyst surface to solve the problem of the charge carrier recombination. Pt is the most active metal for photocatalytic enhancement, which can produce the highest Schottky barrier among the metals that facilitate the electron capture for further photocatalytic reaction (Vorontsov *et al.*, 1999). In particular, supported bimetallic Pt-Ag nanoparticles are of fundamental interest, since Ag has also been found to be effective for photocatalytic activity enhancement. Figures 4.30-4.32 show the specific hydrogen production rates of the bimetallic Pt-Ag-loaded mesoporous-assembled $0.97TiO_2$-$0.03SiO_2$, $0.93TiO_2$-$0.07ZrO_2$, and $SrTi_{0.93}Zr_{0.07}O_3$ photocatalysts with various Pt-Ag loadings prepared by the PCD method. The total bimetallic metal loading was controlled at 1.5 wt.%, whereas the Pt loading decreased from 1.5 to 0 wt.% while the Ag loading conversely increased from 0 to 1.5 wt.%. The results show that the specific hydrogen production rates increased until reaching maximum values of 3.21 $cm^3/h{\cdot}g_{cat}$, 2.11 $cm^3/h{\cdot}g_{cat}$, and 5.37 $cm^3/h{\cdot}g_{cat}$ for the 1.25 wt.% Pt-0.25 wt.% Ag-loaded $0.97TiO_2$-$0.03SiO_2$, the 1.25 wt.% Pt-0.25 wt.% Ag-loaded $0.93TiO_2$-$0.07ZrO_2$, and the 1.25 wt.% Pt-0.25 wt.% Ag-loaded $SrTi_{0.93}Zr_{0.07}O_3$ photocatalysts, respectively. These results clearly indicate an improvement of the specific hydrogen production rates by the bimetallic 1.25 wt.% Pt-0.25 wt.% Ag loading as compared to the monometallic 1.5 wt.% Pt loading. From Table 4.8, the band gap energies of the photocatalysts with bimetallic Pt-Ag loadings are in the following order: $0.93TiO_2$-$0.07ZrO_2$ > $0.97TiO_2$-$0.03SiO_2$ > $SrTi_{0.93}Zr_{0.07}O_3$. Due to the too high band gap energies of the $0.93TiO_2$-$0.07ZrO_2$ photocatalysts with bimetallic Pt-Ag loadings, this possibly led to their low photocatalytic hydrogen production activity. Moreover, as it has been found that the CB level of $SrTiO_3$ provides a higher photopotential than TiO_2 and preferably facilitates hydrogen formation, this may result in the high photocatalytic hydrogen production activity of the bimetallic Pt-Ag-loaded $SrTi_{0.93}Zr_{0.07}O_3$. When considering the physicochemical properties of all the bimetallic Pt-Ag-loaded photocatalysts, the metal dispersion is believed to greatly affect the photocatalytic activity. This can be clearly observed form the maximum photocatalytic hydrogen production activities of the 1.25 wt.% Pt-0.25 wt.% Ag-

loaded photocatalysts, which possessed the highest metal dispersions (Table 4.9). The interactions between the two components in the bimetallic Pt-Ag nanoparticles with their suitable contents may also introduce a significant influence on the neighboring metal atoms as an ensemble effect of agglomerated Pt and Ag nanoparticles, which leads to unique electronic and structural properties of the nanoparticles and improves the photocatalytic activity of the monometallic Pt nanoparticles, as reported by Li *et al.* (2007). From the overall experimental results, the 1.25 wt.% Pt-0.25 wt.% Ag-loaded $SrTi_{0.93}Zr_{0.07}O_3$ can be considered to be the most effective photocatalyst for dye-sensitized hydrogen production in this work.

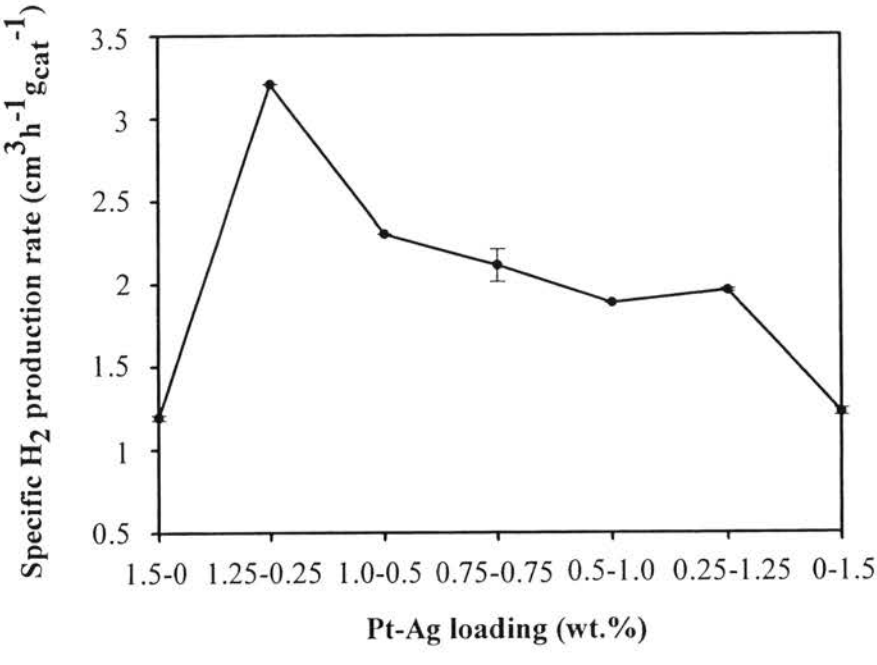

Figure 4.30 Effect of bimetallic Pt-Ag loading on specific H_2 production rate over the mesoporous-assembled $0.97TiO_2$-$0.03SiO_2$ photocatalyst calcined at 500 °C (Photocatalyst, 0.2 g; total reaction mixture volume, 150 ml; DEA concentration, 15 vol.%; E.Y. concentration, 0.1 mM; irradiation time, 5 h).

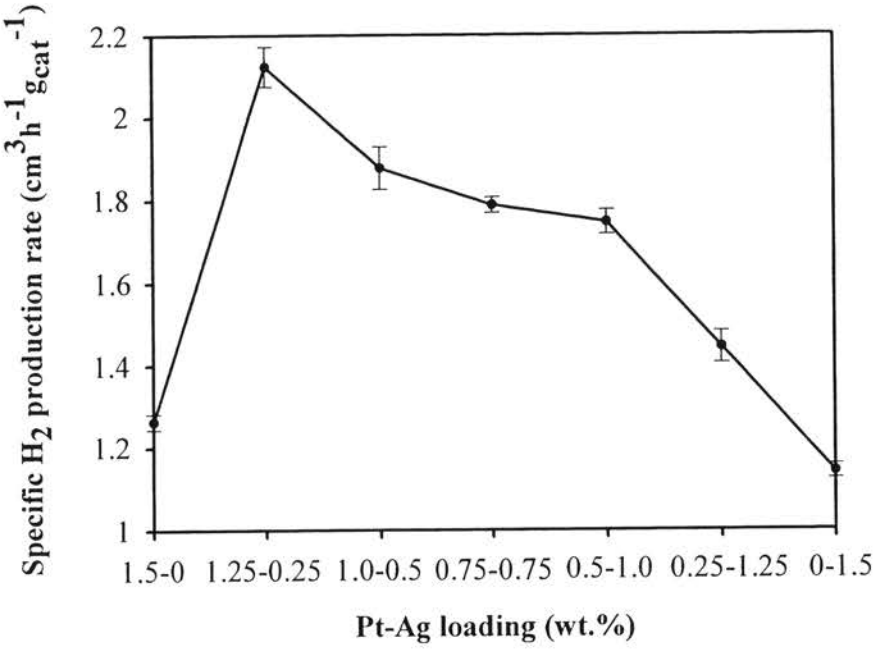

Figure 4.31 Effect of bimetallic Pt-Ag loading on specific H_2 production rate over the mesoporous-assembled $0.93TiO_2$-$0.07ZrO_2$ photocatalyst calcined at 500 °C (Photocatalyst, 0.2 g; total reaction mixture volume, 150 ml; DEA concentration, 15 vol.%; E.Y. concentration, 0.1 mM; irradiation time, 5 h).

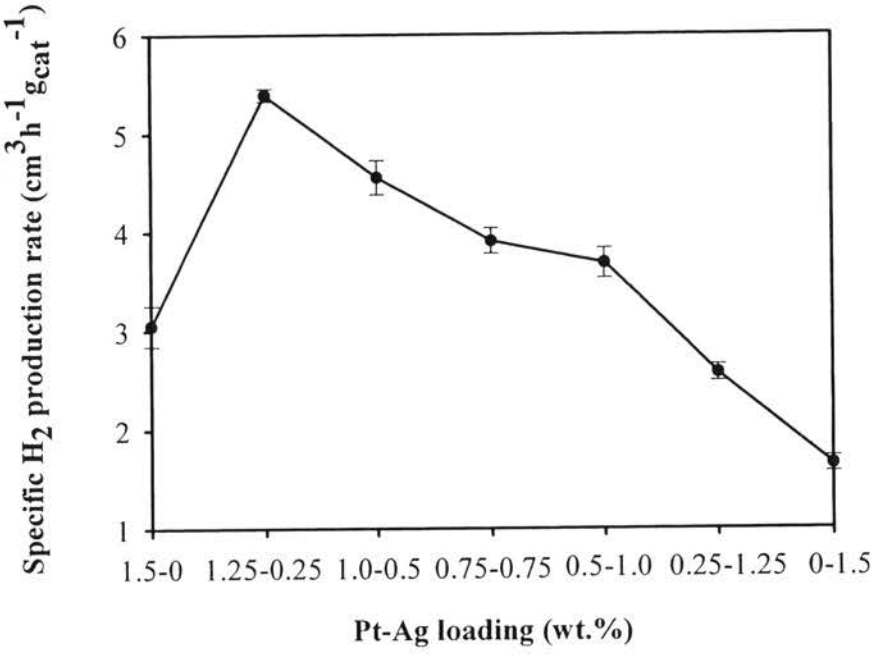

Figure 4.32 Effect of bimetallic Pt-Ag loading on specific H_2 production rate over the mesoporous-assembled $SrTi_{0.93}Zr_{0.07}O_3$ photocatalyst calcined at 700 °C (Photocatalyst, 0.2 g; total reaction mixture volume, 150 ml; DEA concentration, 15 vol.%; E.Y. concentration, 0.1 mM; irradiation time, 5 h).